Nano Energy 141 (2025) 111123

Contents lists available at ScienceDirect

Nano Energy

journal homepage: www.elsevier.com/locate/nanoen

Full paper

A composite bacterial cellulose for enhanced-performance triboelectric and piezoelectric nanogenerators

Sk Shamim Hasan Abir, Charli Smith, Jared Zornitzer, Johnson Samuel *, Semih Akin *

Department of Mechanical, Aerospace and Nuclear Engineering, Rensselaer Polytechnic Institute, Troy, NY 12180, USA

ARTICLE INFO

Keywords:
Bacterial cellulose
Spray coating
Electroless plating
Energy devices
Triboelectric nanogenerator
Piezoelectric nanogenerator
Self-powered sensor
Biomotion sensing

ABSTRACT

Integrating sustainable materials into energy devices, such as triboelectric nanogenerators (TENGs) and piezoelectric nanogenerators (PENGs), offers a promising path towards renewable and eco-friendly energy solutions. Among various sustainable materials, "bacterial cellulose" (BC) stands out for its biocompatibility, affordability, mechanical strength, high surface area and porosity. However, its application in nanoenergy devices is hindered by the challenge of seamlessly embedding an electrically conductive layer (electrode) within BC while preserving its intrinsic properties. This study addresses this hurdle by developing a composite bacterial cellulose (CBC) structure through an innovative manufacturing pathway comprising: (i) spray coating; (ii) electroless copper (Cu) plating; and (iii) freeze drying. The electroless plating step creates a conformal, strongly bonded Cu layer (electrode) on the spray coated surface (i.e., silver nitrate), producing the CBC (i.e., BC with an integrated Cu sublayer). The subsequent freeze-drying step removes moisture from the CBC, while maintaining the mechanical integrity and flexibility. The fabricated CBCs are thoroughly characterized in terms of film thickness, electrical resistance, microstructure, mechanical properties, breathability, and biodegradability. TENG and PENG devices incorporating CBC as the functional tribolayer exhibited 2.1- fold and 4.8-fold improvements in energy harvesting, respectively, compared to control devices. Notably, the TENG with CBC achieved a peak open-circuit voltage of 128 V and a power density of 443.5 $\mu W/cm^2$, while the PENG with CBC recorded 27.2 V and 13.26 $\mu W/cm^2$ with a promising pressure sensitivity of 0.423 V/N. Besides, both devices maintained stable energy harvesting performance over 5000 operational cycles, underscoring their durability and reliability. This work presents a novel CBC structure along with an innovative manufacturing strategy that can pave the way for next generation nanoenergy devices for mechanical energy harvesting, biomotion sensing, and self-powered sensing applications.

1. Introduction

The rapid advancement of electronic technologies—ranging from wearable sensors and implantable medical devices to the internet of things (IoT) and artificial intelligence (AI)—has driven a growing demand for energy harvesting solutions that are lightweight, efficient, and eco-friendly [1–3]. Conventional batteries, constrained by their limited lifespans and recycling challenges, have thus become less appealing as long-term power solutions [4,5]. In response, nanogenerators - particularly triboelectric nanogenerators (TENGs) and piezoelectric nanogenerators (PENGs)- have emerged as compelling technologies for converting ambient mechanical energy into electrical power [6,7]. Their inherent simplicity, scalability, and versatility make them well-suited for powering next-generation electronics in biomedical, environmental, and portable systems. [8–10].

Within the field of nanoenergy devices, the incorporation of sustainable materials into TENGs and PENGs has emerged as a transformative approach to addressing the growing demand for renewable and eco-friendly energy solutions [11–14]. These materials not only contribute to the eco-friendliness of energy devices but also enable tunable properties that can be tailored to specific applications, such as wearable electronics, bio-sensors, and implantable devices [15–17]. Notably, the integration of various sustainable materials (e.g., biopolymers, plant-derived carbon materials, silk fibroin, bacterial cellulose) as functional layers has led to significant performance enhancements in these devices, paving the way for their broader adoption in renewable energy systems and next-generation smart technologies [18–22].

* Corresponding authors.
E-mail addresses: samuej2@rpi.edu (J. Samuel), akins@rpi.edu (S. Akin).

https://doi.org/10.1016/j.nanoen.2025.111123
Received 6 March 2025; Received in revised form 6 May 2025; Accepted 7 May 2025
Available online 8 May 2025
2211-2855/Published by Elsevier Ltd.

"Bacterial Cellulose" (BC), among other sustainable materials, stands out due to its to its excellent mechanical properties, high crystallinity, intrinsic biodegradability, high surface area, and porosity [23,24]. BC primarily has positive charge affinity, due to its abundance of hydroxyl (–OH) groups along the cellulose chains [24]. During repeated contact-separation cycles in TENGs, these hydroxyl groups can donate electrons, leading to a net positive charge accumulation on the BC surface [25,26]. Furthermore, the high crystallinity and well-structured hydrogen-bond networks within BC facilitate steady and efficient charge transfer, thereby enhancing its triboelectric output. In addition to its application in TENGs, BC's unique piezoelectric response—attributed to the aligned glucan chains in its microfibrils and the extensive hydrogen bonding that produces localized polar domains under mechanical deformations—significantly enhances the performance of PENGs [27,28]. Its intrinsic piezoelectricity, coupled with excellent mechanical strength and biocompatibility, enables efficient energy conversion and sustainable energy harvesting, making it an ideal material for advanced PENG applications [29,30].

However, the large-scale deployment of BC in nanoenergy devices (i.e., TENG, PENG) faces several key challenges. A primary hurdle is achieving the seamless integration of an electrically conductive layer (electrode) within BC matrix while maintaining its intrinsic physical and mechanical properties [31,32]. High-strength electrode deposition is vital to ensure efficient charge transfer [33], while issues of adhesion strength, durability, and scalability must be also addressed for practical energy harvesting applications [6,33]. Existing studies have aimed to address these challenges by incorporating functional conductive fillers (e.g., Ag flakes, Ag nanowires, ZnO, barium titanate (BaTiO3), multiwall carbon nanotube (MWCNT), carbon black into the pristine BC to create Composite Bacterial Cellulose (CBC) structures [31,32,34–36]. Integrating CBC structures into TENGs and PENGs has shown significant performance gains [30,37], highlighting their promise for flexible, eco-friendly energy harvesting and smart sensing.

Despite great promise, several key challenges remain for existing CBC materials, including: (i) complex fabrication [29]; (ii) use of toxic reagents [38]; (iii) weak filler-matrix bonding [23]; and (iv) limited scalability for cost-effective production [39]. Addressing these challenges is pivotal to unlock the full potential of CBC in next-generation energy and sensing technologies.

To tackle these challenges, this work introduces a CBC structure, fabricated via electroless Cu plating on pristine BC. This approach eliminates the need for adhesive-backed electrodes (Al or Cu tapes), effectively mitigating interface delamination issues. The Cu-plated layer serves as a durable, robust, and highly conductive electrode, establishing direct contact with triboelectric or piezoelectric layers to minimize charge-transfer losses. Notably, the approach preserves the fibrous architecture of bacterial cellulose without aggressive chemical or physical processing, ensuring enhanced mechanical stability and breathability. The fabricated CBC is characterized in terms of film thickness, electrical resistance, microstructure, mechanical properties, water vapor permeability, and biodegradability. Furthermore, the TENG and PENG devices were designed and fabricated employing CBC as the functional layer and benchmarked against control counterparts. Comprehensive morphological and electrical characterizations reveal promising performance of the CBC-based TENG and PENG devices over conventional copper tape–based BC nanogenerators in terms of conductivity, durability, sensitivity, and power density.

Collectively, this study contributes to literature by introducing the following major innovations:

i. A novel CBC structure developed through an innovative and facile manufacturing pathway.
ii. Durable, robust, flexible, and conductive electrode inscription on the BC surface, serving as functional layer in nano-energy harvesting devices.
iii. Insights into process-structure-property relationships, enabling enhanced performance of nano-energy devices towards eco-friendly sustainable-energy harvesting and biomotion sensing.

2. Materials and methods

Table 1 summarizes the materials used in each process, along with their corresponding vendors and brief descriptions. All materials were used as received without further purification. For the BC synthesis, unpasteurized store-bought Kombucha (*GT's Synergy Raw Kombucha, Gingerade*), containing the bacteria *Bacillus coagulans* (*GBI-306086*), was used. The silver nitrate ($AgNO_3$) powders, diluted in ethanol, were sprayed on the BC surface as the catalyst (seed) material for the subsequent Cu plating process. For the preparation of electroless Cu plating bath, copper sulfate pentahydrate ($CuSO_4{\cdot}5\ H_2O$) was used as the Cu^{+2} source; ethylenediaminetetraacetic acid (EDTA) as the chelating agent; sodium hydroxide (NaOH) as the pH controller; and hydrochloric acid (HCl) as the leaching agent. Formaldehyde (HCHO was employed as the reducing agent to facilitate the deposition of Cu film on the $AgNO_3$-treated BC surface. Further details for each process are provided in Sections 2.1–2.3.

Fig. 1a illustrates the fabrication of CBC, which involves a series of sequential processes as described below:

1) Synthesis of pristine BC as the substrate material
2) Spray coating of $AgNO_3$, serving as the catalyst (seed) material for the subsequent electroless Cu deposition process
3) Electroless Cu plating to create the composite BC by embedding a thin layer of Cu within the pristine BC matrix. This layer functions as a critical component in nanoenergy devices, serving as an active layer as well as back-electrode.

The resulting CBC retains its structural integrity and exhibits promising electrical conductivity, even under severe deformation conditions, as shown in Fig. 1b. The following sub-sections provide detailed description of each process.

2.1. Bacterial cellulose synthesis

The fabrication of bacterial cellulose (BC) follows a traditional fermentation method based on the symbiotic culture of bacteria and yeast according to literature [40]. First, seven cups (1 cup volume equivalent to ~250 mL) of deionized (DI) water were boiled in a beaker. To the boiling water (100°C), five cups of granulated sugar were added, stirring continuously until fully dissolved. Once the sugar was dissolved, four standard black tea bags were steeped in the solution to provide nourishment for the bacteria. The solution was then left to cool to room

Table 1
Materials used in each process.

Process	Material	Vendor	Description
1) BC synthesis	Kombucha	Lab-made	Energy harvesting layer (substrate)
2) Spraying	Silver nitrate ($AgNO_3$) + Ethanol mixture	Sigma Aldrich	Seed (catalyst) material for the ED process
3) Electroless deposition (ED)	Copper (II) sulfate pentahydrate ($CuSO_4{\cdot}5\ H_2O$)	Sigma Aldrich	Source of Cu^{+2} ions
	Ethylenediaminetetraacetic acid (EDTA)	Sigma Aldrich	Chelating agent
	Sodium hydroxide (NaOH)	Sigma Aldrich	pH controlling agent
	Hydrochloric acid (HCl)	Fisher Scientific	Leaching agent
	Formaldehyde (HCHO)	Sigma Aldrich	Reducing agent

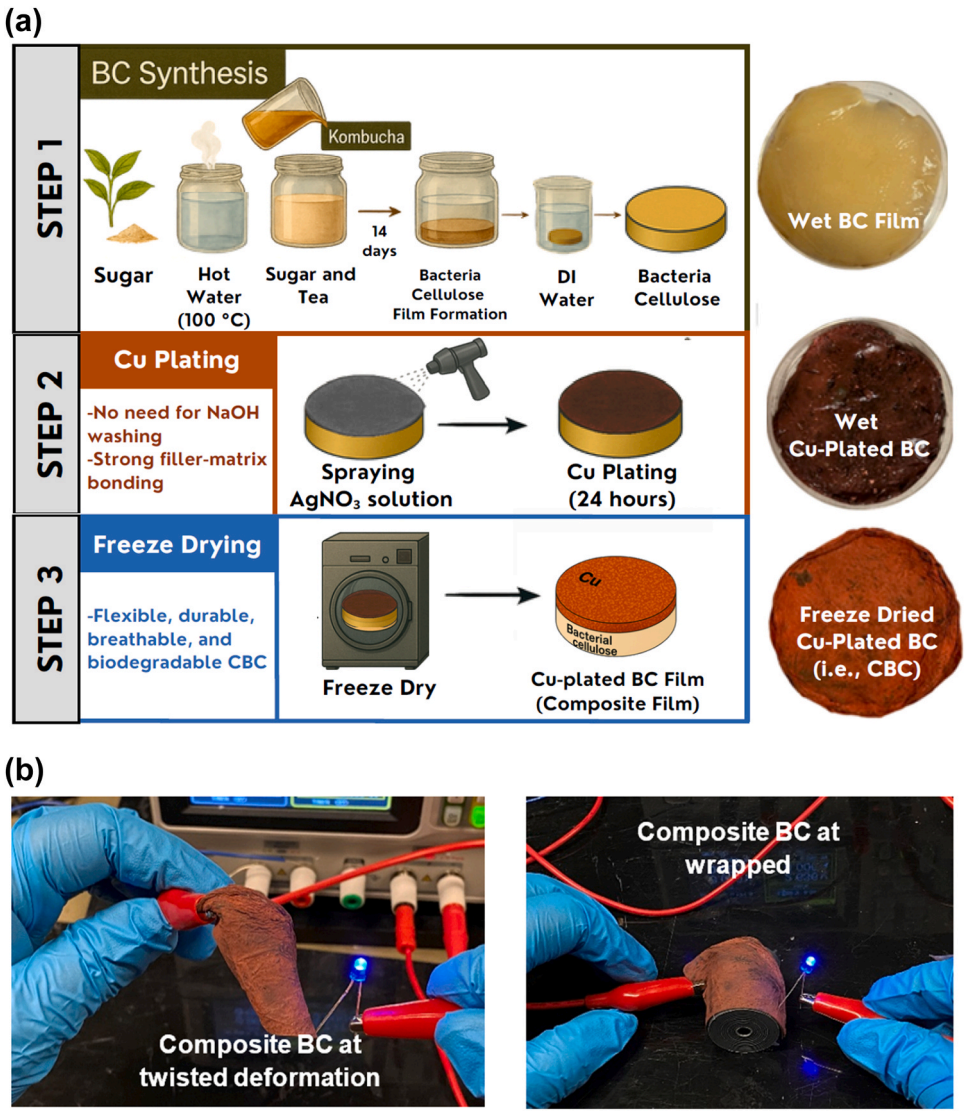


Fig. 1. (a) Schematic diagram of CBC synthesis (left panel) alongside representative images (right panel); (b) Demonstration of the resulting flexible CBC film under various mechanical deformation modes.

temperature. After removing the tea bags, the tea-sugar mixture was transferred into a sterilized glass jar. To introduce the necessary microorganisms, 1 cup of unflavored, unpasteurized store-bought Kombucha (*GT's Synergy Raw Kombucha, Gingerade*), containing the bacteria *Bacillus coagulans* (*GBI-306086*) and the yeast *Saccharomyces boulardii*, was added. These microorganisms were responsible for the fermentation process, where the bacteria synthesized cellulose, and the yeast contributed to the fermentation. The jar was then sealed with a tightly woven cloth secured by a rubber band and stored at room temperature for two weeks (14 days). Over this period, the SCOBY (i.e., Symbiotic culture of bacteria and yeast) formed as a gel-like, rubbery biofilm, which is primarily composed of BC as illustrated in Fig. 1a (top panel). Once the SCOBY formed in the jar, it was carefully removed and cleaned in a large beaker containing DI water. To remove any residual impurities and fermentation by-products from the cellulose film, the SCOBY was soaked in the warm DI water while magnetically stirred at 150 rpm for 30 minutes. After cleaning, the SCOBY was placed onto a sterile petri dish, and circular samples with a diameter of 2.54 cm (1 in.) were carefully cut using a sterilized knife. Each of these 2.54 cm diameter wet samples was then transferred into a separate sterile petri dish, ready for the spraying and electroless Cu plating process.

2.2. Spray deposition of $AgNO_3$

The BC surface was sprayed with $AgNO_3$ solution for two primary reasons: (i) to inhibit the further growth of bacterial colonies, leveraging silver's intrinsic antibacterial properties, and (ii) to act as a seed (catalyst) material for the subsequent ED process. In this regard, the $AgNO_3$ solution was prepared according to a published recipe [41], in which 0.5 mg of $AgNO_3$ dissolved in 2.5 mL of DI water, followed by the addition of 35 mL of ethanol. The prepared solution was sprayed on the target BC surface using an airbrush spray (*Master Airbrush Cool Runner II*) (see Figure S1, Supporting Information). The inlet gas pressure was set to 0.2 MPa (≈ 30 psi), with a nozzle distance of 70 mm, ensuring even coverage of the BC surface with $AgNO_3$. Noteworthy, unlike traditional approaches where BC film is washed with NaOH for 3 to 24 hours [42] to inhibit bacterial growth, our approach remarkably shortens this process while simultaneously enabling the formation of an active layer (i.e., seed layer) for the subsequent electroless Cu plating process.

2.3. Electroless Cu plating

Electroless Cu plating process was carried out by leveraging its ability to deposit Cu uniformly without requiring external electrical

current [41]. This well-established method offers several key advantages, including: (i) high conductivity; (ii) uniform coating thickness; (iii) consistent physical and mechanical properties; (iv) high process throughput; and (v) cost-effectiveness [43] Furthermore, compared to other conductive materials such as silver or carbon-based fillers, Cu offers a favorable balance between performance and cost, particularly for scalable and eco-friendly applications [44,45].

The plating Cu path was prepared based on the published literature [41,46]. The bath of copper sulfate pentahydrate ($CuSO_4{\cdot}5\ H_2O$) solution (concentration 18 gm L^{-1}) was prepared in a 250 mL bottle. Copper sulfate dissociated in water to provide copper ions (Cu^{2+}), which were essential for the plating of copper onto the BC film. To stabilize the copper ions and prevent undesirable side reactions, 48 gm L^{-1} of EDTA was added. EDTA acts as an acid stabilizing agent, binding to any metal ions that may interfere with the copper plating process. To adjust the pH of the solution, 45 gm L^{-1} of NaOH was added; NaOH ensures that the solution maintains an alkaline pH around 12, which is necessary for the electroless plating reaction to proceed efficiently. The optimal value pH range for electroless Cu deposition is reported typically between 10.8–12.5 [43], with some studies indicating that a pH of 12.5–13 may be ideal [47]. At lower pH values, the deposition rate decreases, while excessively high pH can lead to bath instability and precipitation issues [47]. Potassium ferrocyanide (200 mg L^{-1}) was included in the solution to help control the plating rate and prevent the formation of copper precipitates. After the addition of 18 mL L^{-1} of HCl and 200 mL of DI water, the solution was stirred at 400 rpm at room temperature for at least 30 minutes, ensuring complete dissolution and mixing of all chemicals.

Next, the reducing agent (formaldehyde) is added to the prepared bath, and the Cu sulfate-formaldehyde mixture is then poured into a petri dish containing the $AgNO_3$-coated BC sample. This process initiates autocatalytic electroless deposition, in which the Cu^{2+} ions are reduced on the $AgNO_3$-sprayed surface, leading to the formation of a Cu film within the pristine BC matrix, thereby creating the CBC (see Fig. 1a, middle panel). Once the Cu plating is completed, the CBC is then rinsed with DI water to clean off any residual chemicals.

Lastly, the CBC undergoes a freeze-drying (*Labconco, Kansas City, MO, USA*) process to remove the water content while preserving the structural integrity and porosity of the BC (Fig. 1a, bottom panel). The freeze-drying process involves freezing the CBC samples in a dry ice bath to ensure uniform freezing, followed by sublimation under vacuum conditions (0.02 mbar) at −82°C for 24 hours. This process prevents the collapse of the BC structure by directly transitioning water from the solid to the vapor phase, bypassing the liquid state. The low temperature and pressure conditions are critical for maintaining the material's microstructure, which is essential for its subsequent properties, such as porosity, mechanical strength, and surface area [48,49]. To ensure consistency across trials, the experimental setup was standardized by using identical sample preparation methods, freeze-drying parameters, and equipment calibration. Each configuration was tested with three replicates to validate the reproducibility of the results. The freeze-drying process was monitored to confirm the completion of sublimation and desorption phases, ensuring uniform drying across all samples [50,51].

2.4. Characterization

The microstructure of the BC films (i.e., pristine BC and CBC) were analyzed using a Field Emission Scanning Electron Microscopy (FESEM) (*Carl Zeiss supra-55*) with an acceleration voltage of 3–5 kVs. Energy Dispersive X-ray Spectroscopy (EDS) was used with an acceleration voltage of 15 kV. The areal surface roughness (S_a) was measured using an optical profilometer (*Zeta-20*). The attenuated Total Reflectance Fourier Transform Infrared (ATR-FTIR) spectra of the baseline BC and CBC were performed by using a spectrometer (*Bruker, VERTEX 70*) over the 500 cm^{-1} to 4000 cm^{-1} wavenumber range. Mechanical properties of the films (viz., elastic modulus (E), ultimate tensile strength (*UTS*), toughness (U_T), and failure strain (ε_f)) were measured using a Universal Tensile Testing (UTS) machine (*Instron 3345*). Samples (10 mm × 1.2 mm cross-section, 40 mm length) were tested with n = 5 to obtain average values and standard deviations.

For the electrical performance characterization, the resistance of the CBC was measured in static conditions and during bending cycles using a digital multimeter (*Agilent 34405 A*). The open-circuit voltage (V_{oc}) of the nanoenergy devices (TENG, PENG) was obtained using an oscilloscope (*Agilent Technologies DSO1014A*), while the short-circuit current (I_{sc}) was recorded with a current amplifier (*Edmund Optics*) interfaced with the oscilloscope. The load was applied to the energy devices using a programmable pneumatic actuator operating at various frequencies (i.e., 1 Hz, 2 Hz, 3 Hz). Representative image of the pneumatic actuator setup is provided in Figure S2, Supporting Information.

3. Results and discussion

3.1. Film thickness

The thickness of the synthesized pristine BC films was measured over a 21-day period, both before and after freeze-drying (Fig. 2a). The wet films reached an average thickness of 5.48 ± 0.2 mm, which decreased to 1.28 ± 0.07 mm following freeze-drying. A marked slowing of growth emerged after 14 days, at which point the wet films reached 5.17 ± 0.3 mm (1.16 ± 0.06 mm post-freeze-drying). This deceleration is attributed to nutrient depletion (as the bacteria exhaust available sugars) and the accumulation of metabolic by-products, such as organic acids, which can inhibit bacterial metabolism and lower the pH [52,53]. In addition, the thickening film restricts oxygen diffusion into the culture, limiting the aerobic conditions needed for cellulose biosynthesis [54,55]. Furthermore, environmental factors such as temperature variations and ambient microbial competition may reduce bacterial viability over extended cultivation times [56]. These convergent factors collectively account for the observed plateau in BC film thickness beyond the 14-day period. Besides, the freeze dryer and petri dishes utilized in this study allowed for wet BC films up to 5 mm in thickness to ensure efficiently freeze-drying. Based on these observations, wet BC film cultivated for 14 days was selected for all subsequent experiments and characterization studies.

3.2. Electrical performance

The influence of Cu plating duration (ranging from 1 to 48 hours) on the electrical resistance of BC film, both before and after freeze-drying, was examined (Fig. 2b). The initial resistance was relatively high but decreased exponentially with increasing plating time. The lowest resistance values were measured as 0.98 ± 0.22 Ω for wet BC and 32 ± 5.2 Ω for dry BC. It is important to note that these resistance values were obtained using the two-point measurement method, which includes the contact resistance of the measurement electrodes. Following 24 hours of Cu plating, the resistance values for both wet and dry BC appeared to saturation, reaching 1.2 ± 0.36 Ω and 55 ± 11.7 Ω, respectively, before and after the freeze-drying process. To balance plating time and conductivity for electrode fabrication, a 14-day-grown BC film plated with Cu for 24 hours was chosen to create CBC for nanogenerator applications.

The electrical conductivity of the CBC was calculated using Eq. 1, where ρ is the bulk resistivity, L is the gauge length of the sample, w is the width, t is the thickness, and R is the measured resistance obtained via the two-point probe method. After 24-hours of electroless Cu plating, the average electrical conductivity (σ) values were obtained as 378 $S{\cdot}m^{-1}$ for wet CBC and 38.5 $S{\cdot}m^{-1}$ for dry CBC, respectively. Although the electrical conductivity of CBC is lower than that of bulk Cu, it holds a moderate position among studies where BC has been modified to acquire electrical conductivity [57–64].

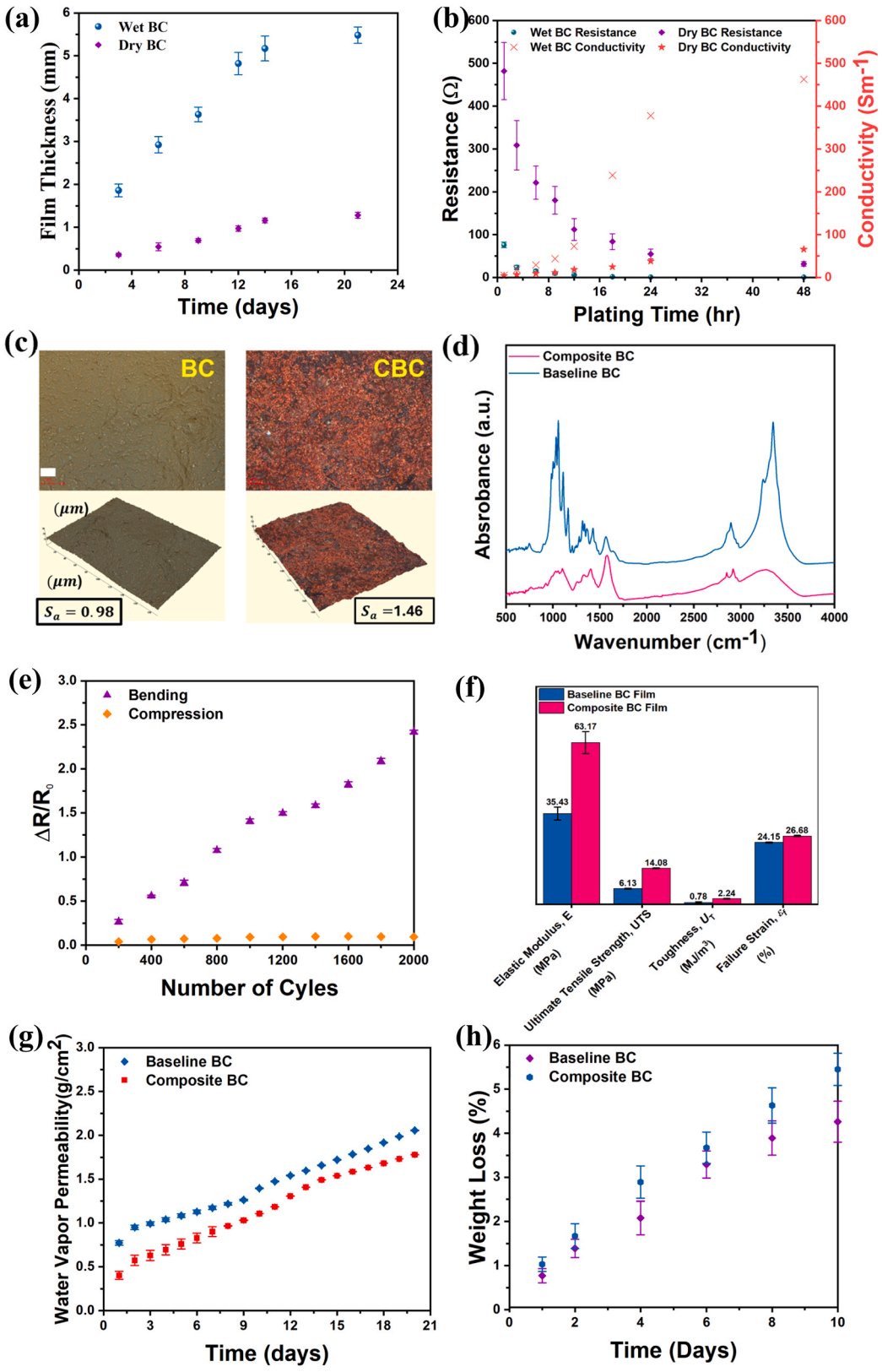


Fig. 2. Comparison of baseline (pristine) BC and CBC: (a) Thickness of wet and dry pristine BC films across varying growth durations; (b) Bulk resistance and conductivity of the wet and dry BCs over the duration of Cu plating; (c) Surface profilometry of baseline BC (left panel) and CBC (right panel) [Scale bar = 15 μm]; (d) ATR-FTIR spectra of baseline BC and CBC; (e) Change of $\Delta R/R_0$ in CBC over 2000 bending and compression cycles; (f) Summary of mechanical properties of baseline BC and CBC; (g) Water vapor permeability of baseline BC and CBC over a period of 20 days; (f) Biodegradability of baseline BC and CBC specimens over a period of 10 days.

$$\sigma = \frac{1}{\rho} = \frac{L}{Rwt} \quad (1)$$

The FESEM micrographs in Fig. 3 compare the microstructures of the baseline (pristine) BC and CBC. As shown in Fig. 3a, the synthesized BC exhibits a dense fibrous surface morphology. Following Cu plating to form CBC, a uniformly distributed Cu layer with Cu particles ranging from approximately 0.3 to 1.0 μm was achieved on the surface (Fig. 3b). In the cross-sectional views (Fig. 3c, d), both the baseline and CBC show similarly fibrous yet dense structures. However, a key feature of the CBC is the presence of a pronounced Cu layer that extends from the surface to sub-surface with a depth of about 20–40 μm, thereby confirming the formation of a Cu–BC composite architecture within the BC matrix. Notably, the presence of Cu layer penetrating the BC matrix facilitates electron transport and contributes to both the stable and durable electrical performance observed. Elemental mapping via EDS further supports these findings (Fig. 3e, f); while the baseline BC contains only carbon and oxygen with no trace of Cu. In contrast, the surface of the CBC is predominantly composed of Cu, confirming successful deposition of Cu within the BC matrix. Besides, as shown in Fig. 2c, the areal surface roughness (S_a) was measured for baseline BC and Cu-plated CBC was 0.98 ± 0.05 μm and 1.46 ± 0.07 μm, respectively, indicating a 49 % increase in the CBC's roughness. Such elevated roughness introduces additional contact points and asperities, thereby potentially enhancing triboelectrification efficiency in TENGs [15,65].

Additionally, the FTIR spectrum analysis of both baseline BC and CBC confirmed the characteristics absorption bands associated with their molecular structures (see Fig. 2**d**). For BC, prominent absorption bands at 3344 cm^{-1} and 2894 cm^{-1} correspond to O–H and C–H stretching vibrations, respectively [66]. Peaks at 1565 cm^{-1}, 1427 cm^{-1}, and 1361 cm^{-1} signify O–H deformation, HCH/OCH bending, and C–H deformation vibrations, while bands at 1159 cm^{-1} and 1107 cm^{-1} highlight asymmetric C–O–C stretching and C–O stretching linked to β-1,4-glycosidic linkages [67,68]. Additionally, vibrations at 1054 cm^{-1} and 1032 cm^{-1} reflect C–OH and C–O–C stretching [69]. In CBC, broad bands between 2800–4000 cm^{-1}, including two new peaks at 2916 cm^{-1}, and 2850 cm^{-1}, indicate O–H and C–H stretching vibrations influenced by Cu nanoparticle integration in BC matrix [70]. A blue shift and reduced intensity of peaks in the 900–1700 cm^{-1} range, except for the strong band at 1571 cm^{-1} (C═O stretching), suggest interfacial bonding between Cu (filler) and the BC matrix. Peaks at 1400 cm^{-1} and 1261 cm^{-1} correspond to C═C stretching in aromatic rings and C–O stretching of esters, while those at 1101, 1054, and 1027 cm^{-1} are attributed to C2–O2, C3–O3, and C6–O6 bond vibrations [71,72].

The effect of Cu-plating temperature on the resulting electrical resistance was also investigated, as shown in Figure S3 (Supporting Information). Elevated temperatures (i.e., 50℃ and 75℃) during electroless Cu plating yielded comparable low resistance values with reduced plating times. At 50°C, a resistance of 32.3 ± 4.4 Ω was achieved within 16 hours, whereas at 75°C, a similar resistance of 33 ± 3.6 Ω was recorded in just 8 hours. These results indicate that higher temperatures accelerate the deposition rate, consistent with trends reported in the literature [43]. Moreover, to assess mechanical durability, CBC

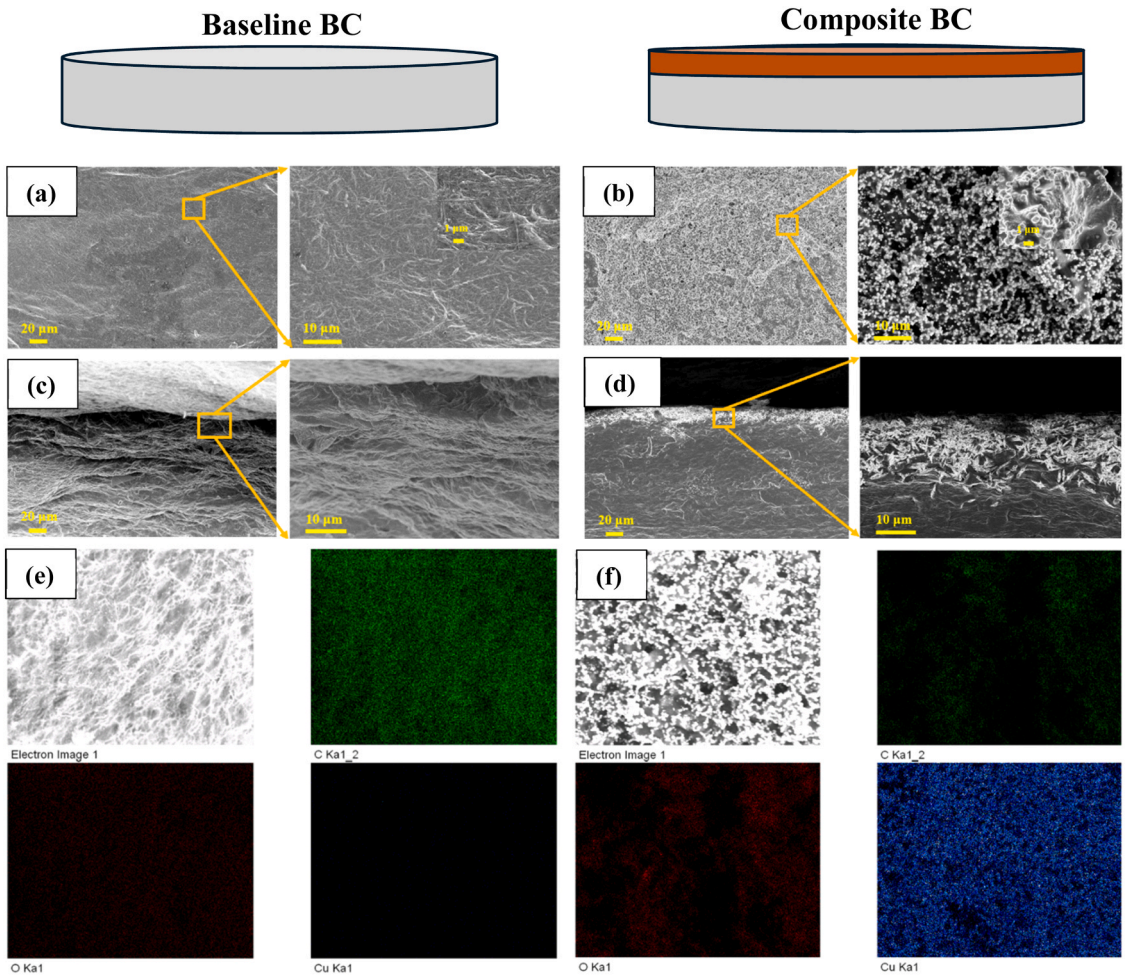


Fig. 3. FESEM micrographs of the top surface of (a) baseline BC and (b) 24 hours Cu plated CBC; Cross- section of (c) baseline BC and (d) 24 hours Cu plated CBC; EDS mapping of the top surface of (e) baseline BC and (f) 24 hours Cu plated CBC.

samples were subjected to 2000 bending cycles (Fig. 2e and Figure S4a-b, Supporting Information). The resistance increased by approximately 2.4-fold relative to the initial value, likely due to the formation of microcracks on the electrode surface, which could disrupt contact within Cu layer. Notably, cyclic tensile loading represents one of the most severe deformation modes, especially considering that TENGs and PENGs typically operate under compressive loading conditions. It is important to highlight that nanoenergy devices primarily experience compressive or sliding deformations—both involving shear stress—rather than bending. However, it should be noted that the developed CBC may experience performance degradation under bending stress—particularly in applications such as flexible electronics and wearable devices, where repeated bending is common.

Under pure compression cycling (Fig. 2e and Figures S4c–d, Supporting Information), the relative resistance change ($\Delta R/R_0$) remained stable (see Video S1), with a maximum recorded value of $\sim 0.1 \pm 0.005$, which is substantially lower than the values observed under tensile loading. This discrepancy can be attributed to the fact that during the 2000 compression cycles, the peak resistance reached only ~3.5Ω, markedly below the typical 55 ± 11.7 Ω resistance of 24-hour Cu-plated dry BC. The reduced resistance is presumably due to compressive forces promoting particle-to-particle contact among the Cu particles, thereby minimizing contact resistance.

Supplementary material related to this article can be found online at doi:10.1016/j.nanoen.2025.111123.

3.3. Mechanical performance

The mechanical properties of both baseline BC and CBC were characterized via tensile testing (see Figure S5, Supporting Information) based on the previous study [53]. As summarized in Fig. 2f, the BC exhibited an elastic modulus (E), ultimate tensile strength (UTS), toughness (U_T), and failure strain (ε_f) are obtained as 35.43 ± 2.54 MPa, 6.13 ± 0.18 MPa, 0.78 ± 0.31 MJ/m^3, and 24.15 ± 0.26 %, respectively. In contrast, the CBC exhibited E, UTS, U_T, and ε_f values of 63.17 ± 4.25 MPa, 14.08 ± 0.17 MPa, 2.24 ± 0.11 MJ/m^3, and 26.68 ± 0.23 %, respectively. The tensile test revealed that the CBC demonstrated approximately 1.8-times higher elastic modulus, 2.3-times higher UTS, 2.8-fold higher toughness, and 1.1 times greater failure strain compared to the baseline BC. This enhancement in mechanical performance can be attributed to multiple factors. First, the Cu plating process likely reinforces the BC matrix, thereby providing additional structural support and reducing the presence of defects, which increases both elastic modulus and ultimate tensile strength [73]. Furthermore, the Cu coating likely to facilitate a more uniform load distribution across the BC surface, mitigating stress concentrations and enhancing overall toughness and failure strain [74,75]. Besides, strong interfacial bonding between the Cu layer and BC fibers was confirmed by the SEM analysis (Figure S6a, Supporting Information), which revealed seamless adhesion of Cu particles across the BC fibers, which is an essential factor for enhanced load-transfer efficiency [73,75].

3.4. Breathability

To assess the breathability of the CBC, water vapor permeability tests were conducted for both baseline and CBC over a 20 days period, in accordance with ASTM E96 standard [76]. Both baseline and CBC, each with a diameter of 2.54 cm, were used to cover a 50 mL centrifuge tube (diameter 2.167 cm) containing water. The initial mass of each BC-covered tube was recorded, and the daily mass loss was measured and converted to water vapor loss per unit exposed area to determine the water vapor permeability. As shown in Fig. 2g, both baseline BC and CBC exhibit similar permeability trend over the course of experiment, illustrating favorable breathability, which is an essential property for applications such as wearable electronics biomedical devices, and air filtration [77,78]. The difference in breathability between the baseline and CBC samples can be attributed to the reduced porosity observed along the sub-surface region of the CBC, as compared to the baseline control group (see Figures S6b-c, Supporting Information). This decreased porosity likely results from the conformal coverage of Cu particles, which partially occludes the microchannels within the BC structure, thereby affecting air permeability.

3.5. Biodegradability

An *in vitro* biodegradability test was performed following the method described in the referenced study [79]. Both baseline BC and CBC dry film were immersed in phosphate-buffered saline (PBS, pH 7.4) at 37 °C to simulate physiological conditions [80]. The dried scaffolds were cut into 20 mm × 20 mm specimens, weighed (w_0), and placed in sealed glass containers containing 20 mL of PBS for up to 10 days. To accelerate the degradation process, 1 % cellulose enzyme was added to the medium. At specified time points (i.e., 1, 2, 4, 6, 8, 10 days), the specimens were removed, washed with distilled water, freeze-dried under vacuum (0.02 mbar) at −82 °C for 24 hours to remove any moisture, and then reweighed (w). The degree of degradation was calculated from the weight loss using the following equation [79]:

$$\text{Weight loss}(\%) = \frac{w_0 - w}{w_0} \text{x} 100 \quad (2)$$

Fig. 2h presents the comparative analysis of the baseline BC and CBC. Both the baseline BC and CBC exhibited similar trends, showing a gradual increase in weight loss (%) over time, as illustrated in Fig. 2h. The maximum weight loss of baseline BC was calculated to be 4.26 ± 0.46 %, while CBC exhibited a slightly higher value of 5.45 ± 0.43 %, indicating enhanced biodegradability. This result can be attributed to the enzymatic degradation of cellulose fibers. In the case of baseline BC, the cellulose enzyme effectively hydrolyzes the cellulose structure, leading to gradual weight loss [81]. However, for the CBC, the presence of the Cu thin layer adds complexity to the degradation process. The enzymatic reaction likely targets the cellulose fibers beneath the Cu layer, weakening the structural integrity of the composite layer. As the cellulose fibers degrade, the Cu layer loses its support and subsequently deplates, further contributing to the overall weight loss. This mechanism accounts for the relatively higher biodegradability of CBC compared to baseline BC, as the concealed degradation beneath the Cu layer accelerates the breakdown of the material. Collectively, the biodegradability analysis confirmed the high level of biodegradability of the developed CBC, thereby demonstrating its promise for environmentally sustainable and recyclable applications.

3.6. Performance evaluation of the nanoenergy devices

3.6.1. Design and fabrication of nanoenergy devices

Triboelectric nanogenerators (TENGs): In this study, as shown in Fig. 4a,various material systems were evaluated for TENG characterization, focusing on contact-separation mode due to its efficient charge transfer and versatility in energy harvesting applications [6,15] In this configuration, the tribo-positive CBC layer repeatedly contacts and separates from a tribo-negative layer (PVDF in Designs I and II, PTFE in Designs III and IV). Upon compression, charges accumulate on the contacting surfaces, when the layers separate, the generated potential difference drives electron flow through the external circuit [82]. Four different TENG configurations (Designs I–IV) were designed and fabricated to examine the performance of electrode materials: in Designs I and III, both electrodes utilize conventional Cu tape, whereas in Designs II and IV, the CBC—with its integral Cu plating—serves as both the tribo-positive layer and its own electrode.

Piezoelectric nanogenerators (PENGs): In parallel, three PENG designs, as presented in Fig. 4b, were investigated to benchmark the performance of CBC based PENGs under compression and release cycles,

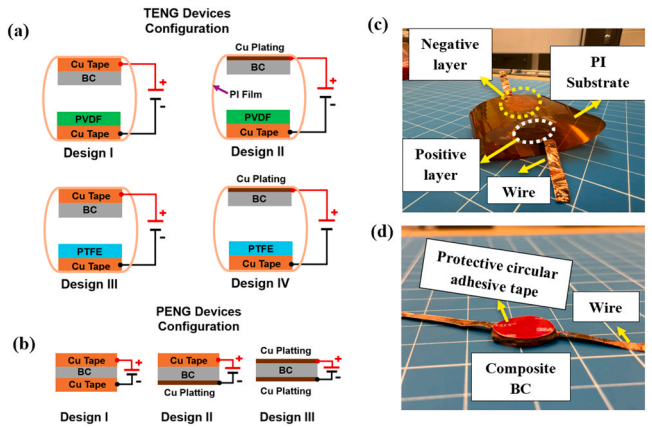


Fig. 4. Schematic of the designed (a) TENGs and (b) PENGs with various material configurations; Representative images of the fabricated (c) TENG (Design IV) and **(d)** PENG (Design III) featuring the CBC as the functional layer/electrode.

comparing them to PENGs made of BC with conventional Cu tape electrodes. All BC based PENGs showed piezoelectric response: (i) upon compression, a piezo-potential is established across the BC surfaces, leading to charge accumulation; (ii) during release, charges flows back through the external circuit, producing alternating current signals [37]. For comparison, Design I features Cu tape on both sides of the BC layer, Design II applies Cu tape on one side while CBC the other side, and Design III employs CBC on both faces. These TENG and PENG configurations (Fig. 4a-d) collectively illustrate how variations in structural modifications (e.g., CBC versus Cu tape) and material selections (e.g., PVDF versus PTFE) were explored.

3.6.2. *TENG performance*

The resultant energy harvesting performance of the TENG devices is presented in Fig. 5. Initially, all four TENG designs were evaluated in terms of open-circuit voltage (V_{oc}) to compare their electrical performance. The triboelectric behavior of both PTFE and PVDF is significantly influenced by their chemical bonds and crystalline phases [83]. PTFE, containing highly electronegative fluorine atoms, demonstrates a strong electron affinity and robust dipole moments [84], thereby enhancing its capacity to capture and retain electrons during triboelectric interactions and resulting in higher charge density [85]. Conversely, PVDF can exist in multiple crystalline phases, among which the β-phase is critically important for its piezoelectric and triboelectric attributes [15]. The β-phase is highly polar, enabling the generation of substantial electrical charges under mechanical stress [86].

As shown in Fig. 5a, the control TENG devices (Designs I and III), which utilize adhesive-based Cu tape electrodes, exhibit maximum V_{oc} of 42 V and 72 V, respectively. This lower performance can be attributed to the inherent drawbacks of adhesive-based copper tape, including inconsistent electrical conductivity and reduced mechanical stability, which arise from the adhesive layer potentially acting as an insulator and disrupting the efficient charge transfer [87,88]. In contrast, CBC-based TENGs—Design II (PVDF) and Design IV (PTFE)—demonstrate markedly enhanced energy harvesting capabilities, achieving maximum V_{oc} values of 88 V and 128 V, respectively, at 3 Hz, corresponding to 2.1-fold and 1.8-fold improvements compared to the control devices. The superior performance of CBC-based TENGs can be attributed to their well-integrated Cu–BC composite architecture, as revealed by FESEM micrographs (Fig. 3b,d), which show a uniformly distributed Cu particle morphology (approximately 0.3–1.0 μm in size) and a pronounced Cu layer extending 20–40 μm into the BC matrix, thereby ensuring greater mechanical stability and more consistent electrical properties.

Recognizing that harsh operating conditions can significantly influence TENG performance, we additionally evaluated the CBC-based device at elevated temperatures (i.e., 50 °C, 80 °C), (see Figure S7, Supporting Information). Notably, the maximum V_{oc} (~128 V) remained comparable to room-temperature values. Although the outputs at 80 °C exhibited moderate fluctuations in peak amplitude, 50 °C measurements remained highly stable, and the overall maximum voltage was effectively maintained. These results confirm that the CBC-based TENG can deliver consistently high electrical outputs under thermal stress, highlighting its potential suitability for long-term deployment in challenging environments. Consequently among these CBC-based devices, the PTFE-based Design IV outperforms its PVDF-based counterpart (Design II), primarily due to PTFE's intrinsically high charge density, favorable surface morphology, and roughness, all of which increase the effective contact area [84,89,90]. Additionally, PTFE's chemical stability and low dielectric loss reduce energy dissipation during charge transfer, thus maximizing energy conversion efficiency [91]. These attributes collectively afford PTFE-based TENGs a distinct advantage, establishing Design IV as the most efficient energy harvester in this investigation.

Given the superior performance of Design IV, it was chosen for further testing. The device was subsequently assessed at three different impact frequencies (1, 2, and 3 Hz) under a 20 psi pressure (Fig. 5b,c). With increasing frequency, both V_{oc} and I_{sc} exhibited similar upward trends; the V_{oc} reached 48 V, 96 V, and 128 V, while the I_{sc} current increased to 9.2 μA, 16 μA, and 22.4 μA at 1, 2, and 3 Hz, respectively. The durability of the device was then examined over 5000 cycles of contact–separation at 3 Hz and 20 psi, demonstrating stable electrical output throughout the test (Fig. 5d,e). In detail, the V_{oc} patterns remained consistant over throughout the test, confirming the device's durability for long-term use. Next, the TENG was connected to a full-bridge rectifier to measure its DC voltage, current density, and power density under varying load resistances ranging from 10 kΩ to 100 MΩ at 3 Hz and 20 psi (Fig. 5f). As predicted by Ohm's law [92], the instantaneous average voltage output gradually increases, whereas the average current density decreased with larger resistive loads. According to the maximum power transfer theorem, the internal impedance of the TENG should match the external load for optimal power output [93]. Indeed, a sharp increase in voltage was observed for load resistances from 1.0 to 5.0 MΩ. Consequently, the power output ($P = V^2/R$) initially rose (Fig. 5g), attaining a peak power density of 443.5 μW/cm^2 at 5.0 MΩ, before subsequently declining at higher resistances. From the Fig. 5i, it can be interpreted that, the power density of 443.5 μW/cm^2 clearly outperofroms the result listed from the literature for BC based TENG devices. To the best of our knowledge, this is of the highest power density achieved by employing BC in TENG applications (see Fig. 5i).

Beyond its electrical performance, the charging capability of the Design IV TENG was also assessed to explore potential applications in energy storage and low-power electronics (Fig. 5h). Using a full-wave bridge rectifier, capacitors of 1.0, 2.2, 3.3, 4.4, and 10.0 μF were charged for 30 s at 3 Hz. The results revealed that as the capacitance increased, the rate of charging gradually decreased. Specifically, the respective maximum voltages reached 2.93, 2.51, 1.64, 1.22, and 0.68 V for the listed capacitances. These findings highlight the practical viability of integrating the Design IV TENG into future energy-harvesting systems aimed at charging and powering small electronic devices.

3.6.3. *PENG performance*

Similar to the TENG investigations, three different PENG configurations (see Fig. 4b) were evaluated in terms of their V_{oc}. As illustrated in Fig. 6a, the PENG device employing a double-sided CBC layer (Design III) exhibited superior performance, generating a V_{oc} of 27.2 V, while control Designs I and II led toonly 5.8 V and 13.7 V, respectively. This indicates that the PENG with CBC remarkbly outperforms the control PENGs, demonstrating ~4.8 and ~2 folds higher performance compared to control configurations.

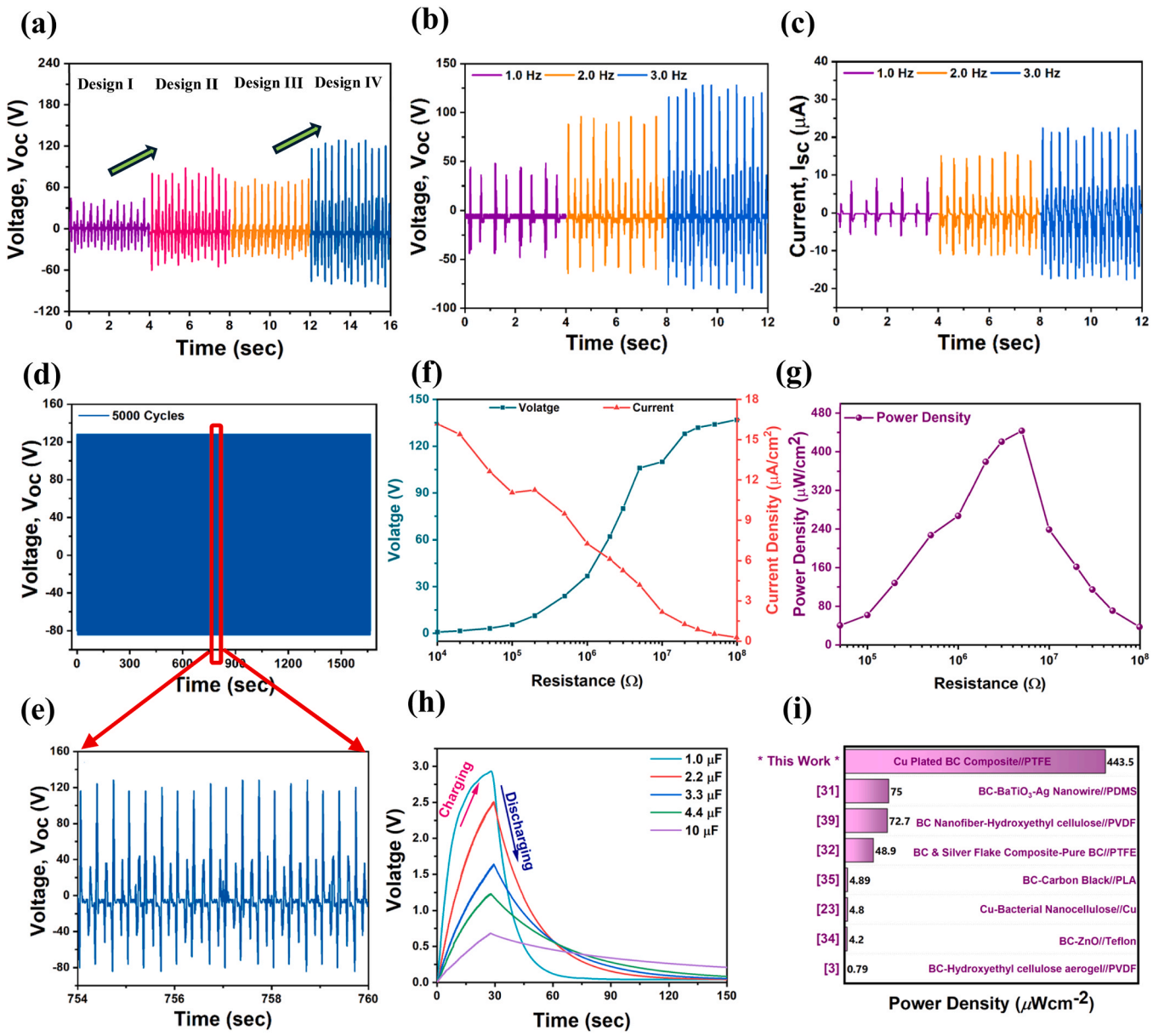


Fig. 5. Energy harvesting performance of the fabricated TENG devices: (a) Open circuit voltage (V_{oc}) of BC with Cu foil as back electrode (control) and CBC (tribo-positive layer) with PVDF and PTFE as tribo-negative layers under ~20 PSI pressure and ~3 Hz load frequency; (b) V_{oc} and (c) short circuit current (I_{sc}) at ~20 PSI and 1–3 Hz load frequency; (d) Durability test and (e) magnified image after 5000 cycles; (f) Average DC voltage, areal current density; and (g) areal power density for various resistive loads (pressure: ~20 PSI; load frequency: ~3.0 Hz); (h) Capacitor charging for 30 seconds using 1.0, 2.2, 3.3, 4.4, and 10 μF capacitors connected to a full bridge rectifier; (i) Comparison of power density of CBC with PTFE TENG and available literature [3,23,31,32,34,35,39].

On account of this enhanced performance, Design III PENG was selected for further characterization. Subsequently, the V_{oc} of the Design III PENG device was measured at varying frequencies (Fig. 6b) and loading pressures (Fig. 6c). At 1, 2, and 3 Hz under a 20 psi load, the maximum recorded V_{oc} values were 10 V, 18.8 V, and 27.2 V, respectively; at 3 Hz with 10, 20, and 30 psi, the V_{oc} progressively rose to 27.2 V, 33.7 V, and 44.4 V, underscoring the device's potential for pressure-sensing applications. In parallel, the short-circuit current (I_{sc}) was also tested at different frequencies under a constant 20 psi load, yielding 1.58, 2.28, and 3.6 μA at 1.0, 2.0, and 3.0 Hz, respectively (Fig. 6d).

To assess the device's durability and repeatability, the PENG output was monitored over 5000 cycles at 3 Hz and 20 psi (Fig. 6e). The magnified view presented in Fig. 6f demonstrates that the V_{oc} remained stable throughout the cycling period. Analogous to the TENG devices, the Design III PENG was also investigated under varying load resistances (10 kΩ to 100 MΩ) at 3 Hz and 20 psi to measure its DC voltage, current density, and power density (Fig. 6g). A trend similar to that observed in the TENG systems emerged, with the notable distinction that the Design III PENG achieved a peak power density of 13.26 μW/cm^2 at a 3.0 MΩ load. Notably, this performance surpasses previously reported BC-based PENG devices, as highlighted in Fig. 6h. To our best knowledge, this presents the highest output performance achieved for a BC-based PENG to date (see Fig. 6h), demonstrating the effectiveness of CBC architecture in enhanced piezoelectric energy harvesting. These findings underscore the promising potential of CBC structure for high performance energy harvesting applications.

Finally, the sensitivity of the proposed PENG was evaluated, and the device demonstrated a sensitivity of 0.423 V/N (Fig. 6i). Along with these advancements in both energy harvesting and sensitivity performance, the results confirm the potential of Design III featuring the CBC for high-performance energy harvesting and sensing applications. Taken

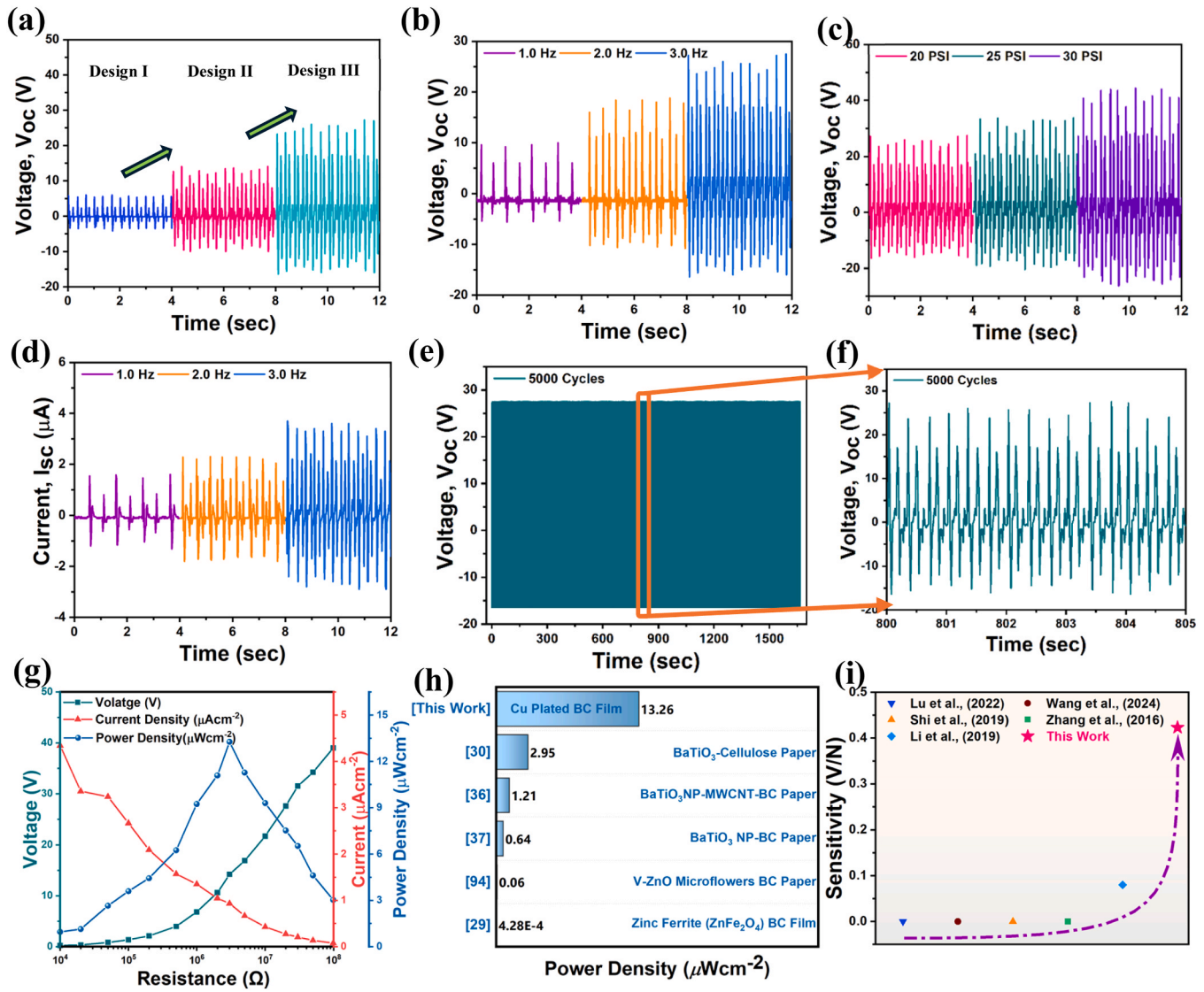


Fig. 6. Energy harvesting performance of the fabricated PENG devices: (a) Open circuit voltage (V_{oc}) of BC with Cu foil as back electrode (control) (Design I), one side CBC (Design II) and both side Cu plated CBC (Design III) PENGs under ~20 PSI pressure and ~3 Hz load frequency; (b) V_{oc} and (d) I_{sc} at ~20 PSI and 1–3 Hz load frequency; (c) V_{oc} at ~20, 25 and 30 PSI and 3 Hz load frequency. (e) Durability test and (f) magnified image after 5000 cycles; (g) Average DC voltage, areal current density, and areal power density for various resistive loads (pressure: ~20 PSI; load frequency: ~3.0 Hz); Comparison of (h) power density and (i) piezoelectric load sensitivity of both side Cu-plated CBC PENG and available literature [29,30,36,37,94,95].

all together, the findings highlight the promising performance of the developed CBC in nanoenergy harvesting and sensing applications.

Table 2 presents a comprehensive benchmark comparison of CBC-based TENGs and PENGs, highlighting their key performance metrics. Notably, the CBC-based TENG and PENG developed in this study demonstrate some of the most promising performance characteristics among reported nanoenergy devices in the literature. These results underscore the potential of CBC-based nanoenergy devices for practical applications and their integration into next-generation energy-harvesting and sensing systems.

Table 3 further provides a detailed benchmarking of cellulose derivative-based TENGs and PENGs, highlighting their key performance metrics. Notably, the nanoenergy devices incorporating the CBC developed in this study exhibit strong potential for energy harvesting, positioning them among the most promising nano-energy devices reported in recent years.

3.7. Applications and prospects

To evaluate the sensing and energy harvesting capabilities of the fabricated devices, we tested the piezoelectric nanogenerator (PENG; design III) and the triboelectric nanogenerator (TENG; design IV), each incorporating CBC. Fig. 7a–c presents the V_{oc} responses of the PENG device under single-finger tapping, hand tapping, and hammering at a load frequency of 1 Hz, yielding maximum voltages of 5.5 V, 13 V, and 26.5 V, respectively. The representative images of these tests are provided in Figure S8 (Supporting Information), with corresponding real-time videos provided in Video S2. The low-intensity single-finger tapping generated a modest 5.5 V, indicating that even minimal mechanical force and deformation can effectively activate the piezoelectric effect, making it suitable for high-sensitivity applications. On the one hand, hand tapping with intermediate force produced a higher output of 13 V, demonstrating the device's ability to amplify energy output proportionally with the applied mechanical load and suggesting its potential use where moderate motion is common. Furthermore, high intensity hammering yielded 26.5 V, highlighting the device's capability to

Table 2
Benchmark comparison of BC-based TENGs and PENGs.

	Contact materials	Fabrication method	Pressure (kPa)	Freq. (Hz)	Contract aera (cm^2)	V_{oc} (V)	I_{sc} (μA/cm^2)	V_{oc}/ Pressure (V/kPa)	I_{sc}/Pressure (μA/kPa)	Ref.
TENG	**CBC and PTFE**	**Electroless Cu plating**	**137.9**	**3**	**5.07**	**128**	**4.42**	**0.93**	**0.16**	**This study**
	Bacterial nanocellulose (BNC) and Cu foil/polyoxymethylene (POM)	Film casting	20.48	10	25	13	0.14	0.63	0.17	[36]
	BC/ZnO and Teflon	Hydrogel	5	6	20	49.6	0.25	9.92	0.98	[34]
	BC/ hydroxyethyl cellulose (HEC) and PVDF	Dip coating	NA	5	4	76.61	2.17	NA	NA	[39]
	BC/HEC and PVDF	Aerogel	44.44	1	2.25	21	0.17	0.47	.01	[3]
	BC/Carbon black/ and PLA	Mold casting	NA	7	16	102.3	0.13	NA	NA	[35]
	BC/BC-Ag nanoflakes double layer and PTFE	Mold casting	274.44	3	9	122	0.91	0.44	0.03	[32]
	BC/AgNWs/BTO and PDMA	Vacuum drying	NA	3	4	87	1.78	NA	NA	[31]
	BC/sodium alginate/BTO and Kapton	Vacuum drying	NA	4	78.5	530.1	0.62	NA	NA	[96]
PENG	**CBC**	**Electroless Cu plating**	**206.8**	**3**	**5.07**	**44.4**	**0.71**	**0.21**	**0.03**	**This study**
	BC/Imidazolium perchlorate (ImClO4)	Hydrogel	31.25	NA	4	0.125	NA	0.004	**NA**	[95]
	BC/BaTiO3/MWCNT	Hydrogel	20	5	1.5	22	0.22	1.1	0.02	[36]
	Cellulose/$BaTiO_3$	Aerogel	80	3	4	15.5	0.83	.19	0.04	[30]
	BC/BaTiO3	Vacuum drying	NA	1	6	14	0.19	NA	NA	[37]
	BC/V-ZnO	Press drying	NA	0.5	NA	1.5	0.08	NA	NA	[94]
	BC/ZnFe2O4	Hydrogel	3.06	5	49	0.53	3.67×10^{-5}	0.17	5.88×10^{-4}	[29]

Table 3
Benchmark comparison of cellulose derivative-based TENGs and PENGs.

	Substrate	Functional material/ Functionalization	Pressure (kPa)	Freq. (Hz)	Contract aera (cm^2)	V_{oc} (V)	I_{sc} (μA/cm^2)	Power density (μW/cm^2)	Ref.
TENG	**Bacterial cellulose**	**Cu**	**137.9**	**3**	**5.07**	**128**	**4.42**	**443.5**	**This study**
	Cellulose nanofiber	Black phosphorus and phytic acid	NA	2	NA	116	0.302	1.67	[97]
	Cellulose nanofibrils	2,2,6,6-Tetramethylpiperidine 1-oxyl (TEMPO)-oxidization	44.44	1	9	104	0.93	15.6	[98]
	Cellulose powder	Carbon nanotube (CNT)	25.46	3	19.64	200.4	0.93	123.7	[99]
	Blend of Cellulose pulp, microcrystalline cellulose and cellulose nanofiber	Blend of Carbon black, carbon nanotubes and graphene nanoplatelets	11.11	10	9	39	0.3	6.0	[100]
	Furan functionalized Sisal microcrystalline cellulose fiber	Maleimide modified CaCu 3Ti4O12 (D-CCTO)	NA	1	4	85	0.8	261	[101]
	Cellulose/graphene oxide aerogel	Grafting with trimethoxy (1*H*,1*H*,2*H*,2*H*-heptadecafluorodecyl) silane	NA	2	NA	180	NA	41.32	[102]
	Cellulose nanofiber	MXene	NA	3.5	0.79	1120	2.23	625	[103]
	Natural wood as Cellulose material	3-chloro−2-hydroxypropyl trimethylammonium chloride (CHPTAC)	NA	5	4	335	2.435	380	[104]
PENG	**Bacterial cellulose**	**Cu**	**206.8**	**3**	**5.07**	**44.4**	**0.71**	**13.26**	**This study**
	Cellulose nanofiber	MXene	70	1.5	10	30.8	0.05	0.13	[105]
	Regenerated cellulose	ZnO	85.7	3	7.04	6.98	0.11	0.73	[106]
	Cotton cellulose	BaTiO3	22.22	3	2.25	3.2	0.11	1.72	[107]
	Cellulose	PLLA	53.67	10	6	10.3	0.04	0.07	[108]
	Cellulose nanofibrils	2,2,6,6-Tetramethylpiperidine 1-oxyl (TEMPO)-oxidization/molybdenum disulfide (MoS2)	NA	0.3	4.5	4.1	0.05	NA	[109]
	Cellulose nanofiber	ZnO	122.28	2.5	3.68	31.2	0.09	1.43	[110]
	Cellulose nanofibrils	MoS2/BaTiO3	NA	NA	4.5	8.2	0.11	NA	[111]

efficiently convert substantial mechanical energy into electrical energy, which is ideal for scenarios involving strong, rapid impacts. This progressive increase in V_{oc} with the rising mechanical input not only reflects the device's dynamic range and adaptability but also highlights its beneficial role in enhancing charge generation efficiency and mechanical resilience.

Supplementary material related to this article can be found online at doi:10.1016/j.nanoen.2025.111123.

Similarly, to explore its potential in biomotion sensing, the TENG device was evaluated under various conditions, including hand clapping, walking, and running (see Fig. 7d-f). When attached to the palm (Fig. 7d), the device recorded a maximum V_{oc} of 59.2 V during regular human clapping. Furthermore, when the device was placed on the shoe sole, it successfully enabled monitoring of human walking (Fig. 7e) and running (Fig. 7f), with maximum recorded voltages of 65.6 V and 108 V, respectively. In each case, distinct voltage signals corresponding to

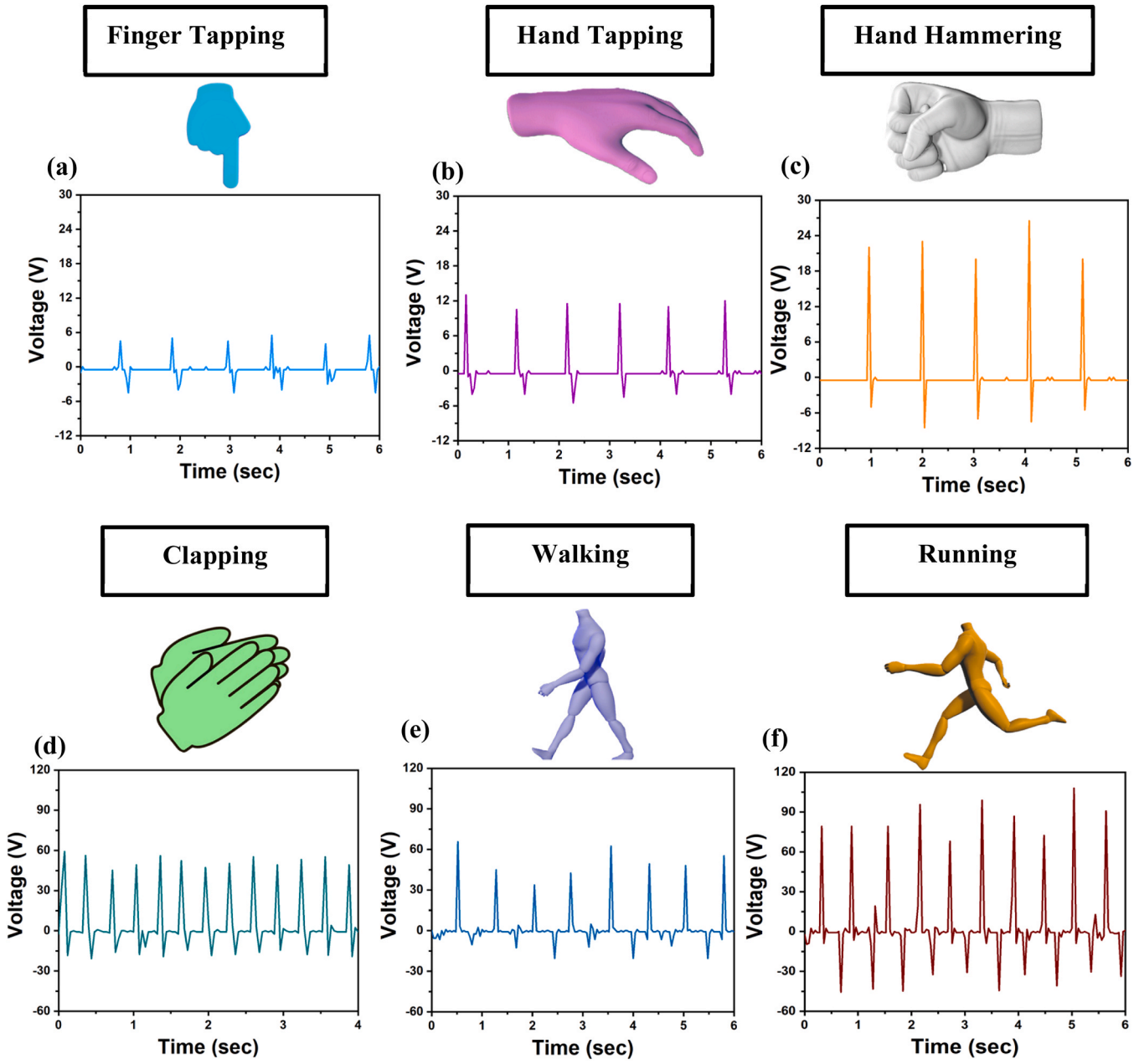


Fig. 7. Demonstration of biomotion sensing using the fabricated nanoenergy devices: Response generated by design III PENG device by (a) single finger tapping; (b) hand tapping; and (c) hand hammering at 1 Hz load frequency. Response generated by design IV TENG device for regular human (d) clapping; (e) walking; and (f) running.

different types of biomotion were generated. These unique signal patterns enable precise biomotion classification, advancing applications in bioelectronics, motion tracking, and wearable sensing. Leveraging these variations enhances the accuracy and responsiveness of smart systems for real-time monitoring, human-computer interaction, and biomedical diagnostics.

Besides, the CBC-based TENG device was connected to full-bridge rectifier, as shown in Fig. 8a (left panel) and Figure S9 (Supporting Information), illuminating a personalized LED circuit consisting of 35 light-emitting diodes (LEDs, each 3 V) arranged to display the initials of *Rensselaer Polytechnic Institute* (see Video S3). Similarly, a commercial calculator (*Casio, Model: fx-991 ES*) was successfully powered using the CBC-based TENG under hand-tapping mode, as shown in Fig. 8b, and further illustrated in the accompanying Video S3. These demonstrations highlight the potential of CBC-TENG for energy harvesting and charging small electronic devices. Taken all together, both the PENG and TENG devices integrated with CBC demonstrate significant potential for energy harvesting and wearable biomotion sensing applications. Their ability to generate distinct voltage signals in response to various mechanical and biomotion inputs not only underscores their dynamic range and adaptability but also highlights their promise for powering next-generation wearable electronics and smart sensing devices.

Supplementary material related to this article can be found online at doi:10.1016/j.nanoen.2025.111123.

4. Conclusion

In this work, we developed a novel CBC structure through an innovative manufacturing pathway that sequentially involves: (i) BC synthesis; (ii) spraying the catalyst material ($AgNO_3$) onto the BC; and (iii)

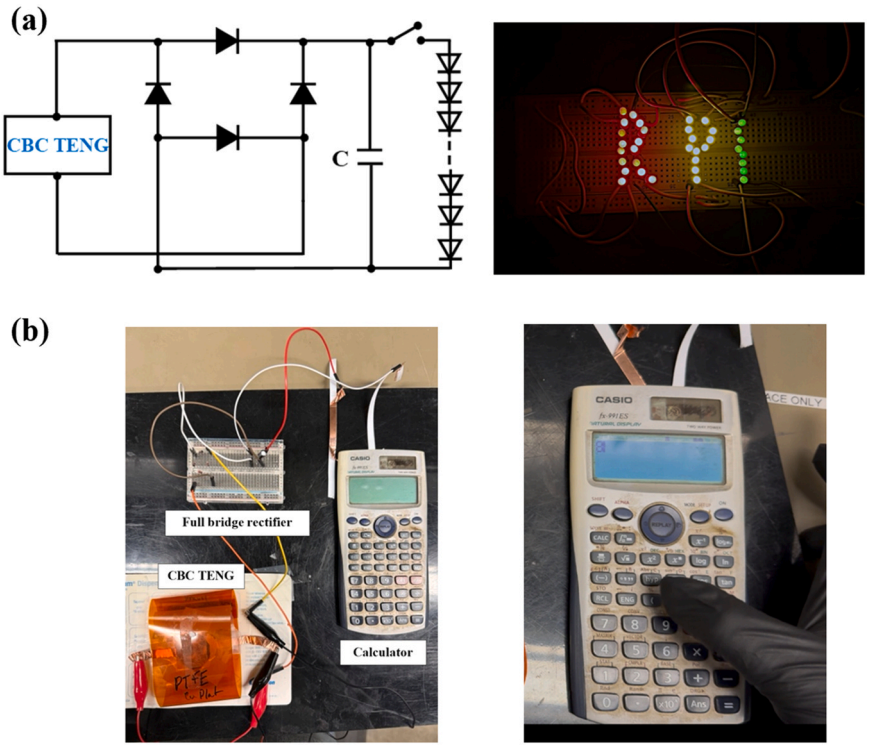


Fig. 8. Demonstration of powering small electronics using the fabricated nanoenergy devices: (a) Schematic of the full bridge rectifier connected to a capacitor for LED illumination (left panel), along with a proof-of-concept demonstration showcasing the LEDs lighting up (right panel); (b) Circuitry image for calculator powering (left panel) and powering a commercial calculator (right panel).

electroless Cu plating to create the CBC. The fabricated CBC was utilized as functional layers in nanoenergy devices, such as TENG and PENG. The following conclusions can be drawn:

- The electroless Cu plating process led the formation of a conductive layer (55 ± 11.7 Ω) within the BC fibrous matrix while preserving its structural morphology and maintaining consistent water vapor permeability.
- The fabricated CBC demonstrated up to a 2.3-fold increase in ultimate tensile strength and a 2.8-fold improvement in toughness compared to baseline BC, highlighting the dual role of Cu layer as both a conductive coating and a reinforcing matrix.
- Among the all tested TENG configurations, configuration IV, which combined CBC and polytetrafluoroethylene (PTFE), yielded the highest V_{oc} of 128 V—1.8 times greater than the control device—and a power density of 443.5 μW/cm^2, surpassing previously reported BC-based TENG performance metrics.
- Simultaneously, the PENG in Configuration III, featuring double-sided Cu-plated BC, achieved a V_{oc} of up to 44.4 V—4.8 times higher than the control PENG—alongside a power density of 13.26 μW/cm^2 and a high sensitivity of 0.423 V/N. These results underscore its strong potential for pressure-sensing applications.
- Both the TENG and PENG devices maintained stable performance over 5000 mechanical cycles, confirming their durability and suitability for practical implementation.
- Biomotion sensing tests confirmed the ability and adaptability of the CBC-based nanonergy devices to effectively convert biomechanical energy into stable electrical signals across a wide range of motions conditions
- Overall, this study underlines the promise of the developed CBC as a key enabler for the next generation of sustainable, high-performance energy-harvesting and sensing devices.

Future research may focus on enhancing the performance of CBC-based nanoenergy devices by incorporating dopants or functional materials into the CBC matrix. Integrating high-electronegativity elements (e.g., fluorinated compounds, metal oxide nanoparticles) could improve charge trapping and surface potential. Additionally, embedding conductive nanomaterials (e.g., graphene, MXene, carbon nanotubes) within CBC matrix may enhance electron transport and mechanical durability. Furthermore, evaluating the long-term stability of these modified structures under varying environmental conditions will be critical for their deployment in energy harvesting and self-powered sensing applications

CRediT authorship contribution statement

Samuel Johnson: Supervision, Resources, Funding acquisition, Conceptualization. **Akin Semih:** Writing – review & editing, Writing – original draft, Validation, Supervision, Resources, Project administration, Methodology, Funding acquisition, Formal analysis, Conceptualization. **Abir Sk Shamim Hasan:** Writing – original draft, Visualization, Validation, Methodology, Investigation, Formal analysis, Data curation, Conceptualization. **Smith Charli:** Methodology, Data curation. **Zornitzer Jared:** Methodology, Data curation.

Supporting information

Figures S1–9 illustrate the following: the spraying of a silver nitrate and ethanol mixture solution, which acted as the seed material for the electroless deposition process; Representative image of the pneumatic actuator setup for nanoenergy device tests; Resistance of the CBC over the duration of Cu plating at different temperatures; The experimental setup for the bending cycle of the films and resistance data of CBC under pure compression for 2000 cycles; Stress-strain curves of BC specimens; Additional FESEM images of BC films; Characterization of CBC-TENG at various temperatures; Representative images of biomotion sensing tests; Representative images of the CBC-TENG driven LED circuit. Videos

S1–S3 present real-time recordings of: resistance cycle tests under compressive loading; energy harvesting and biomotion sensing using the developed nanoenergy devices; and powering small electronic devices with the nanoenergy devices.

Declaration of Competing Interest

The authors declare the following financial interests/personal relationships which may be considered as potential competing interests: S. A., J.S., and S.S.H.A.emih have patent pending to Rensselaer Polytechnic Institute. If there are other authors, they declare that they have no known competing financial interests or personal relationships that could have appeared to influence the work reported in this paper.

Acknowledgement

S.A and J.S acknowledge the internal funding from the Mechanical, Aerospace, and Nuclear Engineering (MANE) Department of Rensselaer Polytechnic Institute. The authors also thank Vrushali Varude (RPI) for her assistance with the FTIR analysis.

Appendix A. Supporting information

Supplementary data associated with this article can be found in the online version at doi:10.1016/j.nanoen.2025.111123.

Data availability

Data will be made available on request.

References

[1] Z.L. Wang, Triboelectric nanogenerators as new energy technology and self-powered sensors - principles, problems and perspectives, Faraday Discuss. 176 (2014) 447–458, https://doi.org/10.1039/c4fd00159a.
[2] F.R. Fan, Z.Q. Tian, Z. Lin Wang, Flexible triboelectric generator, Nano Energy 1 (2012) 328–334, https://doi.org/10.1016/j.nanoen.2012.01.004.
[3] C. Luo, H. Ma, H. Yu, Y. Zhang, Y. Shao, B. Yin, K. Ke, L. Zhou, K. Zhang, M. B. Yang, Enhanced triboelectric nanogenerator based on a hybrid cellulose aerogel for energy harvesting and self-powered sensing, ACS Sustain. Chem. Eng. 11 (2023) 9424–9432, https://doi.org/10.1021/acssuschemeng.3c01369.
[4] W. Liu, M.S. Song, B. Kong, Y. Cui, Flexible and stretchable energy storage: recent advances and future perspectives, Adv. Mater. 29 (2017), https://doi.org/10.1002/adma.201603436.
[5] Z.L. Wang, W. Wu, Nanotechnology-enabled energy harvesting for self-powered micro-/nanosystems, Angew. Chem. - Int. Ed. 51 (2012) 11700–11721, https://doi.org/10.1002/anie.201201656.
[6] S. Akin, T. Chang, S.S.H. Abir, Y.W. Kim, S. Xu, J. Lim, Y. Sim, J. Lee, J.T. Tsai, C. Nath, H. Lee, W. Wu, J. Samuel, C.H. Lee, M.B.G. Jun, One-step fabrication of functionalized electrodes on 3D-printed polymers for triboelectric nanogenerators, Nano Energy 129 (2024), https://doi.org/10.1016/j.nanoen.2024.110082.
[7] S. Shamim, H. Abir, S. Sharma, G. Balasubramanian, J. Samuel, Piezoelectricity in chalcogenide perovskites, Nat. Commun. (2024), https://doi.org/10.1038/s41467-024-50130-5.
[8] T. Kamilya, J. Park, Highly sensitive self-powered biomedical applications using triboelectric nanogenerator, Micromachines 13 (2022), https://doi.org/10.3390/mi13122065.
[9] J.H. Lee, J. Kim, T.Y. Kim, M.S. Al Hossain, S.W. Kim, J.H. Kim, All-in-one energy harvesting and storage devices, J. Mater. Chem. A. 4 (2016) 7983–7999, https://doi.org/10.1039/c6ta01229a.
[10] I. Shabbir, N. Rubab, T.W. Kim, S.W. Kim, Healthcare management applications based on triboelectric nanogenerators, APL Mater. 9 (2021), https://doi.org/10.1063/5.0052605.
[11] M. Venkatesan, W.C. Chen, C.J. Cho, L. Veeramuthu, L.G. Chen, K.Y. Li, M.L. Tsai, Y.C. Lai, W.Y. Lee, W.C. Chen, C.C. Kuo, Enhanced piezoelectric and photocatalytic performance of flexible energy harvester based on CsZn0.75Pb0.25I3/CNC–PVDF composite nanofibers, Chem. Eng. J. 433 (2022) 133620, https://doi.org/10.1016/j.cej.2021.133620.
[12] J.I. Salas, S.S.H. Abir, D. de Leon, I. Serrato, H. Vasquez, K. Lozano, M.J. Uddin, Energy harvesting with thermoplastic polyurethane nanofiber mat integrated with functionalized multiwalled carbon nanotubes, J. Mater. Res. 39 (2024) 2095–2106, https://doi.org/10.1557/s43578-024-01368-8.
[13] M. Ul, K. Sadaf, A. Musa, H. Majumder, S. Shamim, H. Abir, M. Torres, K. Lozano, W. Rahman, M.J. Uddin, Nano Trends Neodymium doped zinc oxide based advanced flexible piezoelectric energy harvester and self-powered biomotion sensor, Nano Trends 8 (2024) 100063, https://doi.org/10.1016/j.nwnano.2024.100063.
[14] S.S.H. Abir, J.E. Trevino, B.B. Srivastava, M.U.K. Sadaf, J.I. Salas, K. Lozano, M. J. Uddin, Synthesis of color tunable piezoelectric nanogenerators using CsPbX3 perovskite nanocrystals embedded in poly(D,L-lactide) membranes, Nano Energy 102 (2022) 107674, https://doi.org/10.1016/j.nanoen.2022.107674.
[15] S.S.H. Abir, M.U.K. Sadaf, S.K. Saha, A. Touhami, K. Lozano, M.J. Uddin, Nanofiber-based substrate for a triboelectric nanogenerator: high-performance flexible energy fiber mats, ACS Appl. Mater. Interfaces 13 (2021) 60401–60412, https://doi.org/10.1021/acsami.1c17964.
[16] W. Li, J. Liu, K. Xia, P. Yang, Z. Zhang, P. Jiao, F. Qu, Z. Xu, Z. He, Dual-mode wireless integrated system for real-time monitoring and early warning of large-scale marine structures, Nano Energy 118 (2023) 108970, https://doi.org/10.1016/j.nanoen.2023.108970.
[17] H. Zhang, Y. Huang, X. Du, Y. Yang, S. Li, D. Fan, X. Xiao, H. Mutsuda, P. Jiao, Self-powered and self-sensing blue carbon ecosystems by hybrid fur triboelectric nanogenerators (F-TENG), Nano Energy 119 (2024) 109091, https://doi.org/10.1016/j.nanoen.2023.109091.
[18] N. Gan, M. Wei, Q. Zhou, K. Dong, B. Gao, Silk fibroin-based triboelectric nanogenerators for energy harvesting and biomedical applications, ACS Appl. Nano Mater. 7 (2024) 8407–8423, https://doi.org/10.1021/acsanm.4c00335.
[19] R. Wang, S. Gao, Z. Yang, Y. Li, W. Chen, B. Wu, W. Wu, Engineered and laser-processed chitosan biopolymers for sustainable and biodegradable triboelectric power generation, Adv. Mater. 30 (2018) 1–8, https://doi.org/10.1002/adma.201706267.
[20] W. Jiang, H. Li, Z. Liu, Z. Li, J. Tian, B. Shi, Y. Zou, H. Ouyang, C. Zhao, L. Zhao, R. Sun, H. Zheng, Y. Fan, Z.L. Wang, Z. Li, Fully bioabsorbable natural-materials-based triboelectric nanogenerators, Adv. Mater. 30 (2018) 1–10, https://doi.org/10.1002/adma.201801895.
[21] M. Zhang, J. Zhang, S. Ran, W. Sun, Z. Zhu, Biomass-derived sustainable carbon materials in energy conversion and storage applications: status and opportunities. a mini review, Electrochem. Commun. 138 (2022) 107283, https://doi.org/10.1016/j.elecom.2022.107283.
[22] P. Jiao, J. Mueller, J.R. Raney, X. (Rayne) Zheng, A.H. Alavi, Mechanical metamaterials and beyond, Nat. Commun. 14 (2023), https://doi.org/10.1038/s41467-023-41679-8.
[23] H.J. Kim, E.C. Yim, J.H. Kim, S.J. Kim, J.Y. Park, I.K. Oh, Bacterial nano-cellulose triboelectric nanogenerator, Nano Energy 33 (2017) 130–137, https://doi.org/10.1016/j.nanoen.2017.01.035.
[24] Y. Song, Z. Shi, G.H. Hu, C. Xiong, A. Isogai, Q. Yang, Recent advances in cellulose-based piezoelectric and triboelectric nanogenerators for energy harvesting: a review, J. Mater. Chem. A. 9 (2021) 1910–1937, https://doi.org/10.1039/d0ta08642h.
[25] A. Chen, C. Zhang, G. Zhu, Z.L. Wang, Polymer materials for high-performance triboelectric nanogenerators, Adv. Sci. 7 (2020) 1–25, https://doi.org/10.1002/advs.202000186.
[26] J. Zhou, H. Wang, C. Du, D. Zhang, H. Lin, Y. Chen, J. Xiong, Cellulose for sustainable triboelectric nanogenerators, Adv. Energy Sustain. Res. 3 (2022), https://doi.org/10.1002/aesr.202100161.
[27] N. Sriplai, R. Mangayil, A. Pammo, V. Santala, S. Tuukkanen, S. Pinitsoontorn, Enhancing piezoelectric properties of bacterial cellulose films by incorporation of MnFe2O4 nanoparticles, Carbohydr. Polym. 231 (2020) 115730, https://doi.org/10.1016/j.carbpol.2019.115730.
[28] R. Mangayil, A.J. Rissanen, A. Pammo, D. Guizelini, P. Losoi, E. Sarlin, S. Tuukkanen, V. Santala, Characterization of a novel bacterial cellulose producer for the production of eco-friendly piezoelectric-responsive films from a minimal medium containing waste carbon, Cellulose 28 (2021) 671–689, https://doi.org/10.1007/s10570-020-03551-6.
[29] Z. Wang, Y. Gu, Y. Xie, C. Zhong, B. Du, M. Xiao, Highly sensitive piezoelectric nanogenerators based on zinc ferrite/bacterial cellulose for vibration fault state identification in power transformers, Nano Energy 131 (2024) 110195, https://doi.org/10.1016/j.nanoen.2024.110195.
[30] K. Shi, X. Huang, B. Sun, Z. Wu, J. He, P. Jiang, Cellulose/BaTiO 3 aerogel paper based flexible piezoelectric nanogenerators and the electric coupling with triboelectricity, Nano Energy 57 (2019) 450–458, https://doi.org/10.1016/j.nanoen.2018.12.076.
[31] H. Yu, Y. Shao, C. Luo, Y. Li, H. zhi Ma, Y. hao Zhang, B. Yin, J. bin Shen, M. bo Yang, Bacterial cellulose nanofiber triboelectric nanogenerator based on dielectric particles hybridized system, Compos. Part A Appl. Sci. Manuf. 151 (2021) 106646, https://doi.org/10.1016/j.compositesa.2021.106646.
[32] S. Sriphan, U. Pharino, P. Pakawanit, T. Bongkarn, W. Vittayakorn, N. Vittayakorn, Simple method for enhancing performance of the bacterial cellulose-based triboelectric nanogenerator by adding conductive interlayer, Integr. Ferroelectr. 238 (2023) 1–12, https://doi.org/10.1080/10584587.2023.2234557.
[33] S. Akin, Y.W. Kim, S. Xu, C. Nath, W. Wu, M.B.G. Jun, Cold spray direct writing of flexible electrodes for enhanced performance triboelectric nanogenerators, J. Manuf. Process 100 (2023) 27–33, https://doi.org/10.1016/j.jmapro.2023.05.015.
[34] S. Jakmuangpak, T. Prada, W. Mongkolthanaruk, V. Harnchana, S. Pinitsoontorn, Engineering bacterial cellulose films by nanocomposite approach and surface modification for biocompatible triboelectric nanogenerator, ACS Appl. Electron. Mater. 2 (2020) 2498–2506, https://doi.org/10.1021/acsaelm.0c00421.
[35] A.L. Freire, L.R. Lima, I.C.M. Candido, L.G. Silva, S.J.L. Ribeiro, E. Carrilho, T. L. Oliveira, L.F.C. de Oliveira, H.S. Barud, H.P. de Oliveira, Metal-free, bio-triboelectric nanogenerator based on a single electrode of bacterial cellulose

modified with carbon black, Nanoenergy Adv. 4 (2024) 110–121, https://doi.org/10.3390/nanoenergyadv4010006.
[36] M. Li, Y. Jie, L.H. Shao, Y. Guo, X. Cao, N. Wang, Z.L. Wang, All-in-one cellulose based hybrid tribo/piezoelectric nanogenerator, Nano Res 12 (2019) 1831–1835, https://doi.org/10.1007/s12274-019-2443-3.
[37] G. Zhang, Q. Liao, Z. Zhang, Q. Liang, Y. Zhao, X. Zheng, Y. Zhang, Novel piezoelectric paper-based flexible nanogenerators composed of BaTiO3 nanoparticles and bacterial cellulose, Adv. Sci. 3 (2015) 1–7, https://doi.org/10.1002/advs.201500257.
[38] B. Park, S.M. Kang, G.W. Lee, C.H. Kwak, M. Rethinasabapathy, Y.S. Huh, Fabrication of CsPbBr3 perovskite quantum dots/cellulose-based colorimetric sensor: dual-responsive on-site detection of chloride and iodide ions, Ind. Eng. Chem. Res. 59 (2020) 793–801, https://doi.org/10.1021/acs.iecr.9b05946.
[39] C. Luo, Y. Shao, H. Yu, H. Ma, Y. Zhang, B. Yin, M.B. Yang, Improving the output performance of bacterial cellulose-based triboelectric nanogenerators by modulating the surface potential in a simple method, ACS Sustain. Chem. Eng. 10 (2022) 13050–13058, https://doi.org/10.1021/acssuschemeng.2c03189.
[40] J. Yang, V. Lagishetty, P. Kurnia, S.M. Henning, A.I. Ahdoot, J.P. Jacobs, Microbial and chemical profiles of commercial kombucha products, Nutrients 14 (2022), https://doi.org/10.3390/nu14030670.
[41] T. Chang, S. Akin, M.K. Kim, L. Murray, B. Kim, S. Cho, S. Huh, S. Teke, L. Couetil, M.B.G. Jun, C.H. Lee, A programmable dual-regime spray for large-scale and custom-designed electronic textiles, Adv. Mater. 34 (2022), https://doi.org/10.1002/adma.202108021.
[42] A.C. Amason, A. Meduri, S. Rao, N. Leonick, B. Subramaniam, J. Samuel, R. A. Gross, Bacterial cellulose cultivations containing gelatin form tunable, highly ordered, laminae structures with fourfold enhanced productivity, ACS Omega 7 (2022) 47709–47719, https://doi.org/10.1021/acsomega.2c04820.
[43] S. Ghosh, Electroless copper deposition: a critical review, Thin Solid Films 669 (2019) 641–658, https://doi.org/10.1016/j.tsf.2018.11.016.
[44] A. Zareei, S. Gopalakrishnan, Z. Mutlu, Z. He, S. Peana, H. Wang, R. Rahimi, Highly conductive copper-silver bimodal paste for low-cost printed electronics, ACS Appl. Electron. Mater. 3 (2021) 3352–3364, https://doi.org/10.1021/acsaelm.1c00345.
[45] Y.J. Yim, S.J. Park, Effect of silver-plated expanded graphite addition on thermal and electrical conductivities of epoxy composites in the presence of graphite and copper, Compos. Part A Appl. Sci. Manuf. 123 (2019) 253–259, https://doi.org/10.1016/j.compositesa.2019.05.021.
[46] S. Akin, C. Nath, M.B.G. Jun, Selective surface metallization of 3d-printed polymers by cold-spray-assisted electroless deposition, ACS Appl. Electron. Mater. 5 (2023) 5164–5175, https://doi.org/10.1021/acsaelm.3c00893.
[47] X. Qin, G. Lin, J. Wang, K. Zheng, X. Feng, Effect of pH value on electroless deposition of copper graphite powders, Prot. Met. Phys. Chem. Surf. 57 (2021) 132–138, https://doi.org/10.1134/S2070205120060192.
[48] D. Nowak, E. Jakubczyk, The freeze-drying of foods — the characteristic of the process course and the effect of its parameters on, Foods 9 (2020) 1–27.
[49] E. Jakubczyk, D. Nowak, Process parameters as tools to intensify the freeze-drying process and modify the sorption properties of the obtained freeze-dried products, Processes 12 (2024) 1932, https://doi.org/10.3390/pr12091932.
[50] Labconco Corporation, A Guide to freeze drying for the laboratory, An Isdustrial Serv. Puplication. (2020) 1–12. ⟨http://www.thermofishersci.in/lit/Labconco-A laboratory guide to freeze drying.pdf⟩.
[51] Ellab, The freeze drying theory and process - things to consider, Ellab White Pap. (2018) 1–16, in: ⟨https://www.ellab.com/Files/Files/White-Papers/The-Freeze-Drying-Theory-and-Process_ellab-whitepaper.pdf⟩.
[52] K. Chlebiej, I. Betlej, The influence of microbiological medium composition on the efficiency of bacterial cellulose synthesis, Ann. WULS For. Wood Technol. 117 (2022) 35–43, https://doi.org/10.5604/01.3001.0015.8701.
[53] A.C. Amason, J.F. Nowak, J. Samuel, R.A. Gross, Effect of atomized delivery of nutrients on the growth characteristics and microstructure morphology of bacterial cellulose, Biomacromolecules 21 (2020) 508–516, https://doi.org/10.1021/acs.biomac.9b01249.
[54] R.R. Singhania, A.K. Patel, Y.S. Tseng, V. Kumar, C.W. Chen, D. Haldar, J.K. Saini, C.Di Dong, Developments in bioprocess for bacterial cellulose production, Bioresour. Technol. 344 (2022) 126343, https://doi.org/10.1016/j.biortech.2021.126343.
[55] J. Wang, J. Tavakoli, Y. Tang, Bacterial cellulose production, properties and applications with different culture methods – a review, Carbohydr. Polym. 219 (2019) 63–76, https://doi.org/10.1016/j.carbpol.2019.05.008.
[56] I. de A.A. Fernandes, A.C. Pedro, V.R. Ribeiro, D.G. Bortolini, M.S.C. Ozaki, G. M. Maciel, C.W.I. Haminiuk, Bacterial cellulose: from production optimization to new applications, Int. J. Biol. Macromol. 164 (2020) 2598–2611, https://doi.org/10.1016/j.ijbiomac.2020.07.255.
[57] T. Sirichaibhinyo, P. Supchocksoonthorn, P. Paoprasert, S. Ummartyotin, The electrical conductivity of a bacterial cellulose and polyaniline composite significantly improved by activated carbon: a nano-based platform for electrodes, ChemEngineering 8 (2024) 87, https://doi.org/10.3390/chemengineering8050087.
[58] D. Gounden, M.N. Pillay, V. Moodley, N. Nombona, W.E. van Zyl, Fabrication and processing of bacterial cellulose/silver nanowire composites as transparent, conductive, and flexible films for optoelectronic applications, J. Appl. Polym. Sci. 140 (2023) 1–16, https://doi.org/10.1002/app.54090.
[59] A.M.R. Rebelo, Y. Liu, C. Liu, K.H. Schäfer, M. Saumer, G. Yang, Carbon nanotube-reinforced Poly(4-vinylaniline)/Polyaniline bilayer-grafted bacterial cellulose for bioelectronic applications, ACS Biomater. Sci. Eng. 5 (2019) 2160–2172, https://doi.org/10.1021/acsbiomaterials.9b00039.
[60] H. Luo, J. Xie, L. Xiong, Y. Zhu, Z. Yang, Y. Wan, Fabrication of flexible, ultra-strong, and highly conductive bacterial cellulose-based paper by engineering dispersion of graphene nanosheets, Compos. Part B Eng. 162 (2019) 484–490, https://doi.org/10.1016/j.compositesb.2019.01.027.
[61] S. Farjana, F. Toomadj, P. Lundgren, A. Sanz-Velasco, O. Naboka, P. Enoksson, Conductivity-dependent strain response of carbon nanotube treated bacterial nanocellulose, J. Sens. 2013 (2013) 741248, https://doi.org/10.1155/2013/741248.
[62] S. Hu, J. Han, Z. Shi, K. Chen, N. Xu, Y. Wang, R. Zheng, Y. Tao, Q. Sun, Z. L. Wang, G. Yang, Biodegradable, super-strong, and conductive cellulose macrofibers for fabric-based triboelectric nanogenerator, Nano-Micro Lett. 14 (2022) 1–20, https://doi.org/10.1007/s40820-022-00858-w.
[63] Z.C. Ling, H.Bin Yang, Z.M. Han, Z. Zhou, K.P. Yang, W.Bin Sun, D.H. Li, H.C. Liu, C.H. Yin, Q.F. Guan, S.H. Yu, Ultrastrong and fatigue-resistant bioinspired conductive fibers via the in situ biosynthesis of bacterial cellulose, NPG Asia Mater. 15 (2023), https://doi.org/10.1038/s41427-023-00461-4.
[64] J. Ye, L. Guo, Y. Feng, F. Sun, T. Zhang, Z. Yang, G. Shen, Z. Zhang, Fabrication of bacterial cellulose-based ATO-PPy nanocomposites as flexible conductive materials, J. Electron. Mater. 49 (2020) 6686–6694, https://doi.org/10.1007/s11664-020-08434-x.
[65] B. Sun, D. Xu, Z. Wang, Y. Zhan, K. Zhang, Interfacial structure design for triboelectric nanogenerators, Batter. Energy 1 (2022) 1–36, https://doi.org/10.1002/bte2.20220001.
[66] C. Babac, T. Kutsal, E. Piski, Production and characterization of biodegradable bacterial cellulose membranes, Int. J. Nat. Eng. Sci. 3 (2009) 19–22.
[67] N. Nurfajriani, A.N. Pulungan, M. Yusuf, N. Bukit, Preparation and characterization of bacterial cellulose from culturation of acetobacter xylinum in coconut water media, J. Phys. Conf. Ser. (2021), https://doi.org/10.1088/1742-6596/1811/1/012070.
[68] N. Atykyan, V. Revin, V. Shutova, Raman and FT-IR Spectroscopy investigation the cellulose structural differences from bacteria Gluconacetobacter sucrofermentans during the different regimes of cultivation on a molasses media, AMB Express 10 (2020), https://doi.org/10.1186/s13568-020-01020-8.
[69] B. Ma, Y. Huang, C. Zhu, C. Chen, X. Chen, M. Fan, D. Sun, Novel Cu@SiO2/bacterial cellulose nanofibers: preparation and excellent performance in antibacterial activity, Mater. Sci. Eng. C. 62 (2016) 656–661, https://doi.org/10.1016/j.msec.2016.02.011.
[70] R. Subbaiya, M.Masilamani Selvam, Synthesis and characterisation of copper nanoparticles using Eupatorium glandulosum extract and their antimicrobial, antioxidant activities, Res. J. Pharm. Biol. Chem. Sci. 6 (2015) 1117–1127.
[71] H. Mahmoudvand, M. Khaksarian, K. Ebrahimi, S. Shiravand, S. Jahanbakhsh, M. Niazi, S. Nadri, Antinociceptive effects of green synthesized copper nanoparticles alone or in combination with morphine, Ann. Med. Surg. 51 (2020) 31–36, https://doi.org/10.1016/j.amsu.2019.12.006.
[72] M. Kačuráková, A.C. Smith, M.J. Gidley, R.H. Wilson, Molecular interactions in bacterial cellulose composites studied by 1D FT-IR and dynamic 2D FT-IR spectroscopy, Carbohydr. Res. 337 (2002) 1145–1153, https://doi.org/10.1016/S0008-6215(02)00102-7.
[73] Z. Al-Maqdasi, R. Joffe, A. Ouarga, N. Emami, S.S. Chouhan, A. Landström, A. Hajlane, Conductive regenerated cellulose fibers for multi-functional composites: mechanical and structural investigation, Materials 14 (2021), https://doi.org/10.3390/ma14071746.
[74] W. Yu, F. Che, V. Liu, M. Lin, J. Lin, B. Rumsey, C. Glancey, Y.C. Ong, H.W. Ng, Substrate copper trace crack characterization and simulation, 2023-May, Proc. - Electron. Compon. Technol. Conf. (2023) 699–705, https://doi.org/10.1109/ECTC51909.2023.00122.
[75] S. Jayalakshmi, P. Venkatesh, P. BalaRamesh, Recent advances in electroless copper deposition – a review, Int. J. Adv. Res. Eng. Appl. Sci. 5 (2016) 1–18.
[76] M.K. Kumaran, Interlaboratory comparison of the ASTM standard test methods for water vapor transmission of materials (E 96-95), J. Test. Eval. 26 (1998), https://doi.org/10.1520/jte11977j.
[77] J. Huang, M. Zhao, Y. Hao, Q. Wei, Recent advances in functional bacterial cellulose for wearable physical sensing applications, Adv. Mater. Technol. 7 (2022) 1–14, https://doi.org/10.1002/admt.202100617.
[78] M. Zhu, Y. Deng, Y. Zheng, X. Hu, W. Xu, R. Xiong, C. Huang, Tribo-charge enhanced and cellulose based biodegradable nanofibrous membranes with highly fluffy structure for air filtration and self-powered respiration monitoring systems, J. Hazard. Mater. 468 (2024) 133770, https://doi.org/10.1016/j.jhazmat.2024.133770.
[79] M. Răpă, C. Zaharia, P.O. Stănescu, A. Căşărică, E. Matei, A.M. Predescu, M. C. Pantilimon, R. Vidu, C. Predescu, H. Cioflan, In vitro degradation of PHB/bacterial cellulose biocomposite scaffolds, Int. J. Polym. Sci. 2021 (2021) 3820364, https://doi.org/10.1155/2021/3820364.
[80] G. Liu, F. Zou, W. He, J. Li, Y. Xie, M. Ma, Y. Zheng, The controlled degradation of bacterial cellulose in simulated physiological environment by immobilization and release of cellulase, Carbohydr. Polym. 314 (2023) 120906, https://doi.org/10.1016/j.carbpol.2023.120906.
[81] I. Leppänen, M. Vikman, A. Harlin, H. Orelma, Enzymatic degradation and pilot-scale composting of cellulose-based films with different chemical structures, J. Polym. Environ. 28 (2020) 458–470, https://doi.org/10.1007/s10924-019-01621-w.
[82] Y.W. Kim, S. Akin, H. Yun, S. Xu, W. Wu, M.B.G. Jun, Enhanced performance of triboelectric nanogenerators and sensors via cold spray particle deposition, ACS Appl. Mater. Interfaces 14 (2022) 46410–46420, https://doi.org/10.1021/acsami.2c09367.

[83] Y. Nurmakanov, G. Kalimuldina, G. Nauryzbayev, D. Adair, Z. Bakenov, Structural and chemical modifications towards high-performance of triboelectric nanogenerators, Nanoscale Res. Lett. 16 (2021), https://doi.org/10.1186/s11671-021-03578-z.
[84] X. Li, Q. Yang, D. Ren, Q. Li, H. Yang, X. Zhang, Y. Xi, A review of material design for high performance triboelectric nanogenerators: performance improvement based on charge generation and charge loss, Nanoscale Adv. (2024) 4522–4544, https://doi.org/10.1039/d4na00340c.
[85] R. Zhang, The opportunities of cellulose for triboelectric nanogenerators: a critical review, Nanoenergy Adv. 4 (2024) 209–220, https://doi.org/10.3390/nanoenergyadv4030013.
[86] T. Bhatta, P. Maharjan, H. Cho, C. Park, S.H. Yoon, S. Sharma, M. Salauddin, M. T. Rahman, S.S. Rana, J.Y. Park, High-performance triboelectric nanogenerator based on MXene functionalized polyvinylidene fluoride composite nanofibers, Nano Energy 81 (2021) 105670, https://doi.org/10.1016/j.nanoen.2020.105670.
[87] C. Wang, X. Wang, Y. Hu, L. Li, Z. Li, H. Wu, Z. Zhao, Investigation on the adhesive contact and electrical performance for triboelectric nanogenerator considering polymer viscoelasticity, Nano Res 14 (2021) 4625–4633, https://doi.org/10.1007/s12274-021-3393-0.
[88] M.A. Elbanna, M.H. Arafa, C.R. Bowen, Experimental and analytical investigation of the response of a triboelectric generator under different operating conditions, Energy Technol. 8 (2020) 1–9, https://doi.org/10.1002/ente.202000576.
[89] J. Xu, Y. Zou, A. Nashalian, J. Chen, Leverage surface chemistry for high-performance triboelectric nanogenerators, Front. Chem. 8 (2020) 1–23, https://doi.org/10.3389/fchem.2020.577327.
[90] D. Liu, L. Zhou, S. Cui, Y. Gao, S. Li, Z. Zhao, Z. Yi, H. Zou, Y. Fan, J. Wang, Z. L. Wang, Standardized measurement of dielectric materials' intrinsic triboelectric charge density through the suppression of air breakdown, Nat. Commun. 13 (2022), https://doi.org/10.1038/s41467-022-33766-z.
[91] F.R. Fan, J. Luo, W. Tang, C. Li, C. Zhang, Z. Tian, Z.L. Wang, Highly transparent and flexible triboelectric nanogenerators: performance improvements and fundamental mechanisms, J. Mater. Chem. A. 2 (2014) 13219–13225, https://doi.org/10.1039/c4ta02747g.
[92] X. Pu, J.W. Zha, C.L. Zhao, S.B. Gong, J.F. Gao, R.K.Y. Li, Flexible PVDF/nylon-11 electrospun fibrous membranes with aligned ZnO nanowires as potential triboelectric nanogenerators, Chem. Eng. J. 398 (2020) 125526, https://doi.org/10.1016/j.cej.2020.125526.
[93] Y. Wu, J. Qu, W.A. Daoud, L. Wang, T. Qi, Flexible composite-nanofiber based piezo-triboelectric nanogenerators for wearable electronics, J. Mater. Chem. A. 7 (2019) 13347–13355, https://doi.org/10.1039/c9ta02345c.
[94] G. Zhang, Q. Liao, M. Ma, F. Gao, Z. Zhang, Z. Kang, Y. Zhang, Uniformly assembled vanadium doped ZnO microflowers/ bacterial cellulose hybrid paper for flexible piezoelectric nanogenerators and self-powered sensors, Nano Energy 52 (2018) 501–509, https://doi.org/10.1016/j.nanoen.2018.08.020.
[95] J. Lu, S. Hu, W. Li, X. Wang, X. Mo, X. Gong, H. Liu, W. Luo, W. Dong, C. Sima, Y. Wang, G. Yang, J.T. Luo, S. Jiang, Z. Shi, G. Zhang, A biodegradable and recyclable piezoelectric sensor based on a molecular ferroelectric embedded in a bacterial cellulose hydrogel, ACS Nano 16 (2022) 3744–3755, https://doi.org/10.1021/acsnano.1c07614.
[96] L. Feng, X. Cao, Z.L. Wang, L. Zhang, A transparent and degradable bacterial cellulose-based film for triboelectric nanogenerator: efficient biomechanical energy harvesting and human health monitoring, Nano Energy 120 (2024) 109068, https://doi.org/10.1016/j.nanoen.2023.109068.
[97] R. Wang, J. Ma, S. Ma, Q. Zhang, N. Li, M. Ji, T. Jiao, X. Cao, A biodegradable cellulose-based flame-retardant triboelectric nanogenerator for fire warning, Chem. Eng. J. 450 (2022), https://doi.org/10.1016/j.cej.2022.137985.
[98] Y. Song, J. Bao, Y. Hu, M. Xu, Z. Yang, Y. Liu, Q. Yang, C. Xiong, Z. Shi, Ultra-porous cellulose nanofibril aerogel films as excellent triboelectric positive materials via direct freeze-drying of dispersion, Nano Energy 103 (2022) 107832, https://doi.org/10.1016/j.nanoen.2022.107832.
[99] Z. Wang, C. Chen, L. Fang, B. Cao, X. Tu, R. Zhang, K. Dong, Y.C. Lai, P. Wang, Biodegradable, conductive, moisture-proof, and dielectric enhanced cellulose-based triboelectric nanogenerator for self-powered human-machine interface sensing, Nano Energy 107 (2023) 108151, https://doi.org/10.1016/j.nanoen.2022.108151.
[100] J. González, A. Ghaffarinejad, M. Ivanov, P. Ferreira, P.M. Vilarinho, A. Borrás, H. Amorín, B. Wicklein, Advanced cellulose–nanocarbon composite films for high-performance triboelectric and piezoelectric nanogenerators, Nanomaterials 13 (2023), https://doi.org/10.3390/nano13071206.
[101] H. Ruan, X. Chen, C. Lv, X. Gu, Z. Zhou, S. Lu, Y. Li, Water-durable, and recyclable dynamic cross-linked cellulose-based triboelectric nanogenerators for energy harvesting, Cellulose 30 (2023) 11425–11437, https://doi.org/10.1007/s10570-023-05568-z.
[102] F. Wang, S. Wang, Y. Liu, S. Ouyang, D. Sun, X. Yang, J. Li, Z. Wu, J. Qian, Z. Zhao, L. Wang, C. Jia, S. Ma, Cellulose nanofiber-based triboelectric nanogenerators for efficient air filtration in harsh environments, Nano Lett. 24 (2024) 2861–2869, https://doi.org/10.1021/acs.nanolett.3c05089.
[103] C. Xing, Y. Tian, Z. Yu, Z. Li, B. Meng, Z. Peng, Cellulose nanofiber-reinforced MXene membranes as stable friction layers and effective electrodes for high-performance triboelectric nanogenerators, ACS Appl. Mater. Interfaces 14 (2022) 36741–36752, https://doi.org/10.1021/acsami.2c10551.
[104] Z. Zhou, Z. Zhang, X. Du, Q.L. Zhang, H. Yang, Dyeing-inspired sustainable and low-cost modified cellulose-based TENG for energy harvesting and sensing, ACS Sustain. Chem. Eng. 10 (2022) 3909–3919, https://doi.org/10.1021/acssuschemeng.1c08095.
[105] Y. Zong, R. Wang, S. Xu, R. Zhang, Z. Zhang, Flexible piezoelectric nanogenerator based on cellulose nanofibril/MXene composite aerogels for low-frequency energy harvesting, ACS Appl. Nano Mater. 6 (2023) 9021–9031, https://doi.org/10.1021/acsanm.3c01649.
[106] X. Song, H. Zou, S. Cao, B. Jiang, M. Li, L. Huang, Y. Zhang, Q. Yuan, Flexible regenerated cellulose/ZnO based piezoelectric composites fabricated via an efficient one-pot method to load high-volume ZnO with assistance of crosslinking, Chem. Eng. J. 475 (2023) 146184, https://doi.org/10.1016/j.cej.2023.146184.
[107] L. Wang, T. Cheng, W. Lian, M. Zhang, B. Lu, B. Dong, K. Tan, C. Liu, C. Shen, Flexible layered cotton cellulose-based nanofibrous membranes for piezoelectric energy harvesting and self-powered sensing, Carbohydr. Polym. 275 (2022), https://doi.org/10.1016/j.carbpol.2021.118740.
[108] L. Xu, Q. kun Zhang, Z. Hu, C. Hua, L. Xue, P. Lu, F. Zhang, Y. Zhang, J. Xiong, Fully biodegradable piezoelectric nanogenerator based on cellulose/PLLA electrospun fibers with high-performance for mechanical energy harvesting, Colloids Surf. A Physicochem. Eng. Asp. 706 (2025), https://doi.org/10.1016/j.colsurfa.2024.135813.
[109] T. Wu, Y. Song, Z. Shi, D. Liu, S. Chen, C. Xiong, Q. Yang, High-performance nanogenerators based on flexible cellulose nanofibril/MoS2 nanosheet composite piezoelectric films for energy harvesting, Nano Energy 80 (2021) 105541, https://doi.org/10.1016/j.nanoen.2020.105541.
[110] Q. Zhu, X. Song, X. Chen, D. Li, X. Tang, J. Chen, Q. Yuan, A high performance nanocellulose-PVDF based piezoelectric nanogenerator based on the highly active CNF@ZnO via electrospinning technology, Nano Energy 127 (2024) 109741, https://doi.org/10.1016/j.nanoen.2024.109741.
[111] M. Xu, T. Wu, Y. Song, M. Jiang, Z. Shi, C. Xiong, Q. Yang, Achieving high-performance energy harvesting and self-powered sensing in a flexible cellulose nanofibril/MoS2/BaTiO3composite piezoelectric nanogenerator, J. Mater. Chem. C. 9 (2021) 15552–15565, https://doi.org/10.1039/d1tc03886a.



Sk Shamim Hasan Abir is a Ph.D. student and currently working as a graduate teaching assistant in the Department of Mechanical, Aerospace, and Nuclear Engineering at Rensselaer Polytechnic Institute (RPI). He received his mechanical engineering master's (2021) from the University of Texas Rio Grande Valley, and bachelor's (2017) from Bangladesh University of Engineering and Technology. His research interests include ceramic sintering, polymer nanocomposite, piezo/triboelectric nanogenerator, flexible electronics, and biosensors. He was awarded the Presidential Graduate Research Assistantship (2019–2021), Margaret Draper Scholarships (2020), and AT&T-UTPA Scholarships (2021).



Charli Smith received her Master of Engineering in Mechanical Engineering from Rensselaer Polytechnic Institute (RPI) in 2024, where she also earned an Advanced Manufacturing Certificate. She previously earned her Bachelor of Science in Biomedical Engineering with a concentration in Biomaterials from RPI in 2023. While at RPI, she was a college athlete on the RPI Softball Team, and was named to the Liberty League All-Academic Team for her excellence in balancing academics and athletics. Her research interests include biological components adapted for the sustainability of piezoelectric and triboelectric nanogenerators, leveraging her background in biomaterials. She is currently a Quality Specialist at Arcellx, a biotechnology company specializing in cell therapy.



Jared Zornitzer graduated with his bachelor's and master's degrees in mechanical engineering from Rensselaer Polytechnic Institute. His research interests include robotics and advanced manufacturing processes.



Dr. Johnson Samuel is a Professor of Mechanical Engineering at Rensselaer Polytechnic Institute (New York, USA). As director of the Nano/Micro-scale Manufacturing and Material Design Lab (NanoM3 Design Lab) at Rensselaer, he leads research and education efforts in the areas of advanced manufacturing and material design. His current interests include additive manufacturing of metal and polymer systems; multi-material co-builds and applied robotics. He is the recipient of the Richard Skalak Award - ASME Bioengineering Division (2024), and U.S. National Science Foundation CAREER award (2014). He currently serves on the ASME Manufacturing Engineering Division's executive committee (2023–2028) and is also an active member of the Society of Manufacturing Engineers.



Dr. Semih Akin is an Assistant Professor of Mechanical Engineering at Rensselaer Polytechnic Institute (New York, USA). He earned his Ph.D. from Purdue University, West Lafayette, USA (2022) and was recognized with Purdue's Outstanding Graduate Student Research Award (2023) and the Lambert Teaching Fellowship (2022). His research focuses on advanced multi-scale manufacturing and surface engineering and with applications in 3D-printed electronics, smart structures, electronic textiles, energy devices, and space manufacturing. His work has earned awards, including Best Paper Awards at *ASME International Mechanical Engineering Congress & Exposition* (IMECE-2024) and *World Congress on Micro and Nano Manufacturing* (WCMNM-2021), Editor's Choice Article in the *Journal of Thermal Spray Technology* (2021), and Outstanding Reviewer recognition by the *ASME Journal of Micro and Nano Science and Engineering* (2024).